Modeling the response of Greenland outlet glaciers to global warming using a coupled flowline-plume model

Johanna Beckmann[1], Mahé Perrette[1], Sebastian Beyer[1,2], Reinhard Calov[1], Matteo Willeit[1], and Andrey Ganopolski[1]

[1] Potsdam Institute for Climate Impact Research, 14412 Potsdam, Germany
[2] Alfred Wegner Institute, 27570 Bremerhaven, Germany

Correspondence: Johanna Beckmannn (beckmann@pik-potsdam.de)

Abstract.

In recent decades, the Greenland Ice Sheet has experienced an accelerated mass loss, contributing to approximately 25 % of contemporary sea level rise (SLR). This mass loss is caused by increased surface melt over a large area of the ice sheet and by the thinning, retreat and acceleration of numerous Greenland outlet glaciers. The latter is likely connected to enhanced submarine melting that, in turn, can be explained by ocean warming and enhanced subglacial discharge. The mechanisms involved in submarine melting are not yet fully understood and are only simplistically incorporated in some models of the Greenland Ice Sheet. Here, we investigate the response of twelve representative Greenland outlet glaciers to atmospheric and oceanic warming using a coupled line-plume glacier-flowline model resolving one horizontal dimension. The model parameters have been tuned for individual outlet glaciers using present-day observational constraints. We then run the model from present to the year 2100, forcing the model with changes in surface mass balance and surface runoff from simulations with a regional climate model for the RCP 8.5 scenario, and applying a linear ocean temperature warming with different rates of changes representing uncertainties in the CMIP5 model experiments for the same climate change scenario. We also use different initial temperature-salinity profiles obtained from direct measurements and from ocean reanalysis data. Using different combinations of submarine melting and calving parameters that reproduce the present-day state of the glaciers, we estimate uncertainties in the contribution to global SLR for individual glaciers. We also perform a sensitivity analysis of the three forcing-factors (changes in surface mass balance, ocean temperature and subglacial discharge), which shows that the role of the different forcing-factors are diverse for individual glaciers. We find that changes in ocean temperature and subglacial discharge are of comparable importance for the cumulative contribution of all twelve glaciers to global SLR in the 21st century. The median range of the cumulative contribution to the global SLR for all twelve glaciers is about 18 mm (the glaciers' dynamic response to changes of all three forcing-factors). Neglecting changes in ocean temperature and subglacial discharge (which control submarine melt) and investigating the response to changes in surface mass balance only leads to a cumulative contribution of 5 mm SLR. Thus, from the 18 mm we associate roughly 70 % to the glaciers' dynamic response to increased subglacial discharge and ocean temperature and the remaining 30 % (5 mm) to the response to increased surface mass loss. We also find a strong correlation (correlation coefficient 0.74) between present-day grounding line discharge and their future contribution to SLR in 2100. If the contribution of the twelve glaciers is scaled up to the total present-day discharge of Greenland, we estimate

the mid-range contribution of all Greenland glaciers to 21st-century SLR to be approximately 50mm. This number adds to SLR derived from a stand-alone ice sheet model (880 mm), that does not resolve outlet glaciers and thus increases SLR by over 50 %. This result confirms earlier studies that the response of the outlet glaciers to global warming has to be taken into account to correctly assess the total contribution of Greenland to sea level change.

1 Introduction

Sea level rise (SLR) is one of the major threats to humanity under global warming, and approximately one-fourth of the recent SLR can be attributed to the Greenland Ice Sheet (GrIS) (Chen et al., 2017). In the future projections of SLR, the GrIS is not only one of the major potential contributors but also a significant source of uncertainty. Two processes are largely responsible for the GrIS contribution to SLR: (1) dynamic mass loss due to retreat and acceleration of outlet glaciers (40 %) and (2) increased surface melt induced by atmospheric warming (60 %) (Khan et al., 2014; Van Den Broeke et al., 2016). The first process which is most pronounced for marine terminating outlet glaciers (Moon et al., 2012), is potentially caused by an increase in submarine melting, which can in turn be attributed to a warming of the subpolar North Atlantic ocean, induced by circulation changes, and increased subglacial discharge (Straneo and Heimbach, 2013). The maximum contribution of increased surface melt is estimated to range between 50 to 130 mm by the year 2100 (Fettweis et al., 2013). Due to the possibility of applying relatively high-resolution regional climate models, confidence in this estimate has increased in the recent years (van den Broeke et al., 2017). The contribution of the dynamic mass loss, however, remains highly uncertain because processes related to the response of marine terminating Greenland glaciers are still not properly represented in the contemporary GrIS models (Straneo and Heimbach, 2013; Khan et al., 2014; Goelzer et al., 2017).

The principal objective of this paper is to quantify the response of marine terminating outlet glaciers to future submarine melting and to analyze whether the impacts of ice-ocean interaction on SLR are comparable to long-term changes in surface mass balance (SMB).

In order to assess Greenland's contribution to future sea level rise, several different model strategies have been proposed. The most common method is to use three-dimensional ice sheet models, tuned to present-day conditions, and apply future climate change projections based on global or regional climate models. However, such models still have relatively coarse spatial resolution and cannot properly resolve most of the outlet glaciers that terminate in Greenland's fjords. Peano et al. (2017) investigated the 5 biggest ice streams and outlet glaciers in Greenland with a 3D ice-sheet model on a resolution of 5 km Seddik et al. (2012) and Gillet-Chaulet et al. (2012) included improved model physics by using a full-Stokes approach and refined resolution over fast flow regions with adaptive mesh techniques. Their setup however, did not yet allow to simulate glacier retreat. Most of the ice-sheet simulations also do not describe the interaction between glaciers and the ocean explicitly, but in some cases, for instance in Fürst et al. (2015), ocean melting is parameterized indirectly by increasing the basal sliding factor as ocean temperature increases. For the RCP scenario 8.5, they calculated a SLR between 155 and 166 mm at the year 2100 for the entire ice sheet applying atmospheric and oceanic forcing. For regional settings, 3D models with a simple ocean melting parameterization were applied to study the historical (last 20 -30 years) retreat of Jakobshavn Isbrae (Muresan and

Khan, 2016; Bondzio et al., 2017). A more advanced treatment of submarine melt rate was used by Vallot et al. (2018). They coupled a plume model based on the Navier-Stokes equations with a full-Stokes ice sheet model. With this off-line coupling, glacier dynamics for one melt season were simulated for Kronebreen Glacier in Svalbard.

Another method, followed by Nick et al. (2013), is to simulate single outlet glaciers individually using a one-dimensional (1D) flowline model. Nick et al. (2013) performed simulations for four outlet glaciers that collectively drain about 22 % of the total solid ice discharge of the Greenland Ice Sheet. Assuming proportionality between the future contribution to SLR and present-day ice discharge, Nick et al. (2013) scaled up results obtained from four glaciers to the total estimate of all Greenland outlet glaciers, which resulted in a range between 65 and 183 mm by the year 2100. Taking this one step further, Goelzer et al. (2013) used the results from Nick et al. (2013) in a 3D coarse-resolution ice sheet model. They applied the 1D glacier thinning and grounding-line retreat scenarios as an external, pre-calculated forcing in the grid cells at the ice sheet boundary. Since only four glaciers had been simulated in the 1D model, they mapped the forcing from the original glaciers onto all other Greenland's marine terminating outlet glaciers with a nearest neighbour approach. The incorporation added only 8 to 18 mm SLR on top of the stand-alone 3D ice sheet model simulation. Goelzer et al. (2013) argued that the rather small contribution compared to Nick et al. (2013) is caused by the full retreat of the small marine terminating glaciers in the 3D ice simulations within in a short timescale. When fully retreated, they do not experience any ice-ocean interaction any more. This loss of ice-ocean interaction, however, is neglected by the upscaling-method from Nick et al. (2013) and therefore leads to higher numbers of total SLR.

Since we are especially interested in the impacts of ice-ocean interactions on glacier dynamics and want to investigate numerous glaciers, we followed an approach similar to Nick et al. (2013) but for different glacier-types and with one notable improvement: for calculations of the vertically distributed submarine melt, we use a turbulent plume parameterization following Jenkins (2011). According to this parameterization, the submarine melt rate depends not only on ambient water temperature in fjords but also on seasonally varying subglacial discharge, shape and angle of the glacier tongue. The first idealized simulations of a coupled flowline-plume model were carried out by Amundson and Carroll (2018) by using the maximum melt rate as a frontal ablation factor to account for undercutting plus calving of tidewater glaciers, demonstrating the potential impact of the subglacial discharge on glacier dynamics. While their study emphasizes the importance of subglacial discharge, their model setup does not allow for the evolution of floating tongues. Thus, we follow a different approach (section 2) to simulate the glacier profile more realistically.

We perform simulations for 12 representative Greenland glaciers (compared to four in Nick et al. (2013)). This enabled us to test the assumption used in Nick et al. (2013) that the contribution of individual Greenland outlet glaciers to SLR is proportional to their present-day discharge and therefore the total contribution of Greenland outlet glaciers can be obtained by scaling up contribution of individual glaciers proportionally to the entire present-day discharge of all outlet glaciers. In particular we derived a proportional factor between present-day grounding line discharge and future SLR using results of simulations for all twelve glaciers. We also estimated the uncertainties in the contribution of Greenland glaciers to SLR resulting from uncertainties in calving and ocean melt parameters and ocean warming.

The paper is structured as follows. First, we describe the coupled flowline-plume model, then how the input data were pre-processed together with the experimental setting and climate change scenarios. Finally, we present the results of our model simulations for present day and future scenarios.

2 The coupled flowline-plume model

Most of Greenland's outlet glaciers terminate in fjords that are connected to the ocean. Inside these fjords, observations of upwelling plumes along the edges of glaciers have drawn attention to the potential importance of submarine melting. Consequently, considerable efforts in the modeling of submarine melt rate have been undertaken by using high-resolution 3D and 2D ocean general circulation models that are tuned to or parameterized after the buoyant-plume theory (Sciascia et al., 2013; Xu et al., 2013; Slater et al., 2015; Cowton et al., 2015; Carroll et al., 2015; Slater et al., 2017). However, such models are computationally too expensive and therefore impractical for simulating the response of the entire GrIS to climate change on centennial timescales. At the same time, recent studies demonstrate that the simple line plume model by Jenkins (2011) is an adequate tool to simulate plume behavior (Jackson et al., 2017) and to determine submarine melt rates for marine terminated glaciers (Beckmann et al., 2018). Since the plume model is significantly less computationally expensive than 3D ocean models, it represents an alternative approach to introduce ice-ocean interaction into the GrIS model and still maintain the model's ability to perform a large set of centennial-scale experiments. Simulating the glacier dynamics with 3D ice sheet models requires very high spatial resolution ($\ll 1$ km) resulting in high computational cost (e. g. Aschwanden et al., 2016) and so far they cannot be used for centennial timescales. To reduce the computational cost we use instead a depth- and width- integrated one-dimensional ice flow model (Enderlin and Howat, 2013; Nick et al., 2013) coupled to a line plume model (Beckmann et al., 2018). Unlike Amundson and Carroll (2018), who used the maximum melt rate as a frontal ablation factor for tidewater glaciers, we take into account the entire profile along the submerged part of the outlet glacier to calculate the submarine melt rate with the plume model (1).

2.1 Glacier model

The governing equations of the 1D glacier model (Fig. 1) include mass conservation:

$$\frac{\partial H}{\partial t} = -\frac{1}{W}\frac{\partial(UHW)}{\partial x} + \dot{B} - \dot{M}, \tag{1}$$

where H is ice thickness, t is time, U is the vertically averaged horizontal ice velocity, W is the width and x is the distance from the ice divide along the central flowline. $\dot{B}$ and $\dot{M}$ are the surface mass balance and the submarine melt rate of the glacier.

The conservation of momentum involves a balance between longitudinal stress, basal shear stress and lateral stress on the one hand, and driving stress on the other:

$$2\frac{\partial}{\partial x}\left(H\nu\frac{\partial U}{\partial x}\right) - A_s\left[(H - \frac{\rho_w}{\rho_i}h_b)U\right]^q - \frac{2H}{W}\left(\frac{5U}{EAWW_s}\right)^{\frac{1}{3}} = \rho_i gH\frac{\partial h_s}{\partial x}, \tag{2}$$

where h_s denotes the ice surface height, h_b the depth of glacier below sea-level, ρ_i and ρ_w the ice and sea water density, respectively. The sliding law follows Nick et al. (2010) with the basal sliding coefficient A_s and the velocity exponent q, and

the lateral stress involves a non-dimensional width-scaling parameter W_s. The lateral stress term likewise used by e.g. Nick et al. (2013); Enderlin and Howat (2013); Schoof et al. (2017), and originally derived by Van Der Veen and Whillans (1996), is necessary to account for lateral resistance in fast-flowing, laterally-confined glaciers typical for Greenland. Finally, the rate factor A and the enhancement factor E determine the viscosity ν

$$5 \quad \nu = (EA)^{\frac{1}{3}} \left| \frac{\partial U}{\partial x} \right|^{-\frac{2}{3}}. \tag{3}$$

Calving occurs when surface crevasses propagate down to the water level (Nick et al., 2013). Crevasses depth d_s is calculated from the resistive stress $R_{xx} = 2 \left(\frac{1}{A} \frac{\partial U}{\partial x} \right)^{1/3}$, as ice stretches, and can be enhanced by freshwater depth d_w:

$$d_s = \frac{R_{xx}}{\rho_i g} + d_w \frac{\rho_0}{\rho_i} \tag{4}$$

where ρ_0 is the freshwater density. The glacier front continuously advances over time, as the accumulated flux leaving the last
10 grid cell is recorded and the calving front is advanced whenever the accumulated volume reaches the volume of a grid cell (assuming same thickness). Glacier front advance and calving are the two competing processes that determine the calving front position.

The boundary condition at the top of the glacier catchment is $U(x = 0) = 0$. At the calving front x_{cf} (Fig. 1, b), the balancing of the longitudinal stress with the hydrostatic sea water pressure and the incorporation of the flow law of ice yields
15 longitudinal stretching

$$\left. \frac{\partial U}{\partial x} \right|_{x=x_{cf}} = EA \left[\frac{\rho_i g H}{4} \left(1 - \frac{\rho_i}{\rho_w} \right) \right]^3. \tag{5}$$

The model employs a stretched horizontal grid with a horizontal resolution of 100 meters, where velocity is calculated at mid-points. At each time step of 3.65 days, the grid is stretched to keep track of the grounding line position, which is determined by the flotation criterion

$$20 \quad H_{\text{float}} \leq |z_b| \frac{\rho_w}{\rho_i}, \tag{6}$$

where z_b is the bedrock depth. Glacier thickness H and bedrock depth z_b of each cell interface are determined by linear interpolation between the cell centered values. Grid stretching is performed so that there is always a cell edge at the interpolated grounding line position (x_{gl} in Fig. 1). The new calving front position is determined so that the total glacier volume is not modified by interpolation. For every new point in the interior, model variables are interpolated from previous grid. The first
25 grid point at the ice divide remains unchanged. If points on the new ice grid lie outside the ice domain of the previous ice grid, as it is typically the case for the last ice cell before the calving front, ice thickness from the last grid cell is extended to the new ice cell (the calving front advances).

The code is written is FORTRAN, following the numerical procedure of Enderlin et al. (2013). The main differences compared to their original matlab code[1] is that we include a subgrid-scale treatment of the calving front boundary, and an improved
30 treatment of the submarine melting.

---

[1]available at https://sites.google.com/site/ellynenderlin/research

2.2 Plume model

The plume model equations account for a uniformly distributed subglacial discharge along the grounding line of a glacier , and contain the evolution of the plume thickness D, velocity V, temperature T and salinity S along the direction of the plume.

$$q_s' = \dot{e} + \dot{m} \tag{7}$$

$$(q_s V)' = D \frac{\Delta \rho}{\rho_0} g \sin(\alpha) - C_d V^2 \tag{8}$$

$$(q_s T)' = \dot{e} T_a + \dot{m} T_b - C_d^{\frac{1}{2}} V \Gamma_T (T - T_b) \tag{9}$$

$$(q_s S)' = \dot{e} S_a + \dot{m} S_b - C_d^{\frac{1}{2}} V \Gamma_S (S - S_b) \tag{10}$$

The volume flux of the plume $q_s = DU$ (expressed per unit length in the lateral direction, i.e. $\mathrm{m^2 s^{-1}}$) is described by equation (7). It can increase by the entrainment of ambient seawater $\dot{e}$ and by melting $\dot{m}$ of ice from the glacier front. Equation (8) describes the balance between buoyancy flux and the drag $C_d U^2$ of the glacier front. The buoyancy flux is proportional to the relative density contrast $\frac{\Delta \rho}{\rho_0}$ between plume water and ambient water in the fjord (subscript a). This density contrast is linearly parameterized as $\beta_S (S_a - S) - \beta_T (T_a - T)$. The drag also results in a turbulent boundary layer (subscript b) at the ice-water interface, where melting occurs, and heat and salt is exchanged by (turbulent) conduction-diffusion. The temperature T and salinity S of the plume (Eq. 9,10) are determined by the entrainment of ambient water and the addition of meltwater, as well as by conduction fluxes at the ice-water interface (i.e. between boundary layer and plume). The entrainment rate is calculated as $\dot{e} = E_0 U \sin(\alpha)$, proportional to plume velocity and glacier slope, with the entrainment coefficient E_0.

The submarine melt rate along the path of the plume $\dot{m}$ is determined by solving the equations of heat and salt conservation at the ice-water interface:

$$\dot{m} L + \dot{m} c_i (T_b - T_i) = c C_d^{\frac{1}{2}} V \Gamma_T (T - T_b) \tag{11}$$

$$\dot{m} (S_b - S_i) = C_d^{\frac{1}{2}} V \Gamma_S (S - S_b) \tag{12}$$

where T_i and S_i, c_i are the temperature, salinity and the specific heat capacity of the ice and c the specific heat density for sea water. At the ice water interface the freezing temperature T_b is approximated as a linear function of depth Z ($Z < 0$) and salinity of the boundary layer S_b:

$$T_b = \lambda_1 S_b + \lambda_2 + \lambda_3 Z \tag{13}$$

with $Z = Z_0 + x \cdot \sin(\alpha)$, where Z_0 is the depth (negative) at the grounding line ($x = 0$). The algorithm for solving the set of equations and a list of all parameter values are provided in Beckmann et al. (2018).

The plume is a 1D model and therefore can neither simulate variability across the calving front (Fried et al., 2015), nor account for fjord wide circulation (Slater and Straneo, 2018) across and outside plumes. However, the width-averaged melt rates - as

required for the 1D glacier model- can be simulated with the 1D plume model (Beckmann et al., 2018). We set the entrainment parameter E to 0.036, as suggested by Beckmann et al. (2018). Since the plume model in some cases underestimates and in others overestimates submarine melt rates (Beckmann et al., 2018), we also scale the simulated melt rate profile by a constant factor β, which we treat as an additional tuning parameter within the range 0.3 - 3 possibly different for each glacier (see

5 section 4.1). The plume model employs a fine spatial resolution of about 1 m.

2.3 Coupling between glacier and plume model

As mentioned in the beginning of this section, the submarine melt rate profile is calculated along the entire glacier profile in contact with the ocean (tidewater glacier or with floating tongue, Fig. 1 a and b) and converted into a thickness loss for each of these glacier cells.

10 Submarine melting volume flux is calculated for each cell and is applied as a vertical thinning rate on the floating tongue $(x_{g+1}...x_c)$, or on the last grounded cell (x_g) in the case of tidewater glaciers (no floating tongue). The melt rate $\dot{m}$ is integrated from the grounding line (position x_{gl}) along the bottom face of the floating tongue (if any), and along the calving face (position x_{cf}) up to sea level (Fig. 1), or to the top height of the risen plume (which can stop below sea level). The total submarine melt rate over the glacier tongue (if any) for one outlet glacier is given by

$$15 \quad M = \int \dot{m}(s)\,ds = \int\limits_{x_{gl}}^{x_{cf}} \dot{m}(h_b(x)) \cdot (\cos\alpha)^{-1} dx + \int\limits_{h_b(x_{cf})}^{0} \dot{m}(z)dz, \tag{14}$$

where s is the distance coordinate along the tongue bottom and the vertical calving face, h_b denotes bottom ice elevation, and $\cos\alpha$ is the variable tongue slope (calculated from the relation $\tan\alpha = \frac{\partial h_b}{\partial x}$). The integral is partitioned over various glacier cells (or only one cell (x_g) in the case of a tidewater glacier, where the first integral term is zero since $x_{gl} = x_{cf}$). This total submarine melt rate, in a cell by cell basis, is substituted in (the discrete form) of equation (1):

$$20 \quad M_i = \int\limits_{x_{i-\frac{1}{2}}}^{x_{i+\frac{1}{2}}} \dot{m}(s)\,ds + \varepsilon_i \int\limits_{h_b(x_{cf})}^{0} \dot{m}(z)dz, \tag{15}$$

where ε_i is 1 if i represents the last ice cell $(x_i = x_c)$, or 0 otherwise. The submarine melt rate $\dot{M}$ per units of length for each glacier cell (dx) in Eq. 1 is

$$\dot{M_i} = \frac{M_i}{dx} \tag{16}$$

If there is no floating tongue, submarine melting is applied to the last grounded cell, otherwise it is applied starting from the

25 first floating cell.

Thus the submarine melt rate reduces the thickness of the glacier cell. A reduced thickness at the first floating cell or last grounded cell leads to grounding line retreat since the grounding line position is determined by interpolation of the ice thickness

above flotation at each time step. Calving front retreat can be reached by melting/thinning the last floating ice cell completely or by calving, which increases with thinning.

Since the plume model does not allow for negative values of α, its minimum value is set to 10^{-6}. If the plume already ceases before reaching the calving front x_{cf}, we numerically introduce a minimal background melting determined by the last melt rate value before the plume ceased. At the calving front we calculate a 2nd plume that starts at $h_b(x_{cf})$ with the initial minimum default discharge value of $10^{-6}\,\mathrm{m^3\,s^{-1}}$ to assure a background frontal melting.

Subglacial discharge Q for each glacier was computed off-line from the output of simulations with the ice sheet model SICOPOLIS (Calov et al., 2018) which includes explicit treatment of basal hydrology (Section 3.3). It is applied to the line plume (Fig. 2), assuming a uniform distribution of subglacial discharge along the width of the grounding line: $q_s = Q(W)^{-1}$. It is assumed that plume properties (velocity, temperature, salinity, and thickness) adapt instantaneously to changes in the glacier's shape, subglacial discharge, temperature and salinity profiles of ambient water. The glacier and plume model exchange information at every time step of the glacier model (Fig. 2).

3 Model Input

To simulate the response of the glacier-plume model to future global warming we considered the potential changes of surface mass balance (SMB) and submarine melting. To this end, for each glacier, we derived data sets for three forcing factors from the year 2000 till 2100: spatially distributed SMB (section 3.3), subglacial discharge (section 3.3) and fjord water temperatures (section 3.4). For changes in SMB we used anomalies from the simulation with the regional climate model MAR, forced by global GCM MIROC5 for the RCP8.5 scenario. In our previous study (Calov et al., 2018) we used the same SMB changes to force the 3D ice-sheet model SICOPOLIS. Now we use results of this simulation to compute the subglacial discharge for each glacier from simulated surface runoff. Changes in ocean temperature were included by applying a linear warming trend, derived from several different CMIP5 models. On every time step the three forcing factors were provided as data-input and forced the glacier-plume model (Fig. 2). While for each glacier the future evolution of the subglacial discharge and ocean temperature were firmly prescribed in the data-sets, the SMB-input was interactively corrected for the surface elevation feedback and thus considered the glacier surface height on each time step. The upcoming subsections describe the choice of glaciers, how the geometry for the 1D model was derived and how the corresponding forcing factors were determined and applied.

3.1 The choice of glaciers

In this study we modeled twelve well-studied Greenland outlet glaciers of different sizes and located in different regions of Greenland (Fig. 3). One criterion for this selection was that the glaciers should represent different types of ice flows and different environmental conditions. We also included small marine terminating glaciers to assure a more realistic upscaling (Goelzer et al., 2013). Besides that, for most of the chosen glaciers, Enderlin and Howat (2013) estimated submarine melting to calving ratios (grounding line mass flux lost by submarine melting divided by mass loss of calving) which were used as an additional constraint on the choice of modeling parameters.

3.2 Glacier geometry

For each individual glacier, bedrock elevation and width were determined by analysing cross-sections taken at regular intervals along the glacier flow, generally covering a large portion of the glacier catchment area (Perrette et al., in prep). In each cross-section, the procedure comes down to calculating a flux-weighted average for bedrock elevation, ice velocity U and thickness H, and choosing the glacier width W such that the flux F through the cross-section is conserved, i.e. $W = F/(UH)$. We used the BedMachine v2 data for bedrock topography (Morlighem et al., 2014). Fjord bathymetry was extended manually by considering available data (Mortensen et al., 2013; Schaffer et al., 2016; Dowdeswell et al., 2010; Syvitski et al., 1996; Rignot et al., 2016). For ice velocity we use data from Rignot and Mouginot (2012). The resulting glacier profiles are depicted in Fig. 6.

3.3 Subglacial discharge and glacier surface mass balance

To force the plume model, we used monthly averaged subglacial discharge. Subglacial discharge represents the sum of basal melt (melt under the grounded ice sheet), water drainage from the temperate layer and surface runoff. The former two sources were computed directly by the ice sheet model SICOPOLIS (Calov et al., 2018). In reality surface runoff can travel along the ice surface until it either reaches an existing connection to the bedrock (e.g. crack) or it accumulates in a supraglacial lake that eventually drains, making a new connection. However, these processes are complex and still poorly understood. This is why in the relatively coarse (5 km) resolution ice sheet model (Calov et al., 2018), these small-scale processes were neglected and it was assumed that runoff penetrates directly down to the bedrock. The surface runoff and SMB anomalies for future scenarios are taken from experiments with the regional climate model MAR (Fettweis et al., 2013) and corrected for the future surface elevation change (Calov et al., 2018). The entire basal water flux (runoff, basal melt, and water from the temperate layer) was routed by the hydraulic potential using a multi-flow direction flux routing algorithm, as described in Calov et al. (2018). All water transfer was assumed to be instantaneous. Water that passes through the boundary of the prescribed SICOPOLIS ice mask was assigned to the closest glacier within a maximum distance of 50 km. This maximum distance is necessary in areas where only few named glacier positions are available (mostly in the South of Greenland) and the distance between glaciers is large. For most of the coastline, especially in the area of our selected glaciers, this distance had no effect on the results. We did not separately study the uncertainty in subglacial discharge related to this approach, but rather accounted for this uncertainty implicitly through the uncertainty of the scaling coefficient β for the submarine melt rate (see section 4.1).

In our future scenarios, when simulating subglacial discharge, we accounted for changes in surface runoff, basal melt, and ice sheet elevation. The routing end-points, that determine the amount of subglacial discharge for each glacier, however, were set constant to the present-day position of the ice sheet margin. For neighbouring glaciers with a competing catchment area, a strong ice sheet retreat may strongly affect the distribution of the subglacial discharge between those glaciers (Lindbäck et al., 2015). This effect was not included in this study.

In this study, we used a single scenario for future surface runoff and SMB change, namely, a simulation with the regional model MAR nested in the global GCM MIROC5 model forced by the RCP 8.5 scenario. Among the CMIP5 models, MIROC5 simulates climate change which led to a medium contribution of GrIS to future SLR (Calov et al., 2018). To correct for global climate model biases in surface runoff and SMB, we used an anomalous approach by adding future anomalies in surface runoff and SMB simulated by MAR nested into the MIROC5 model to the reference climatology (reference period 1961-1990) simulated by MAR forced by ERA reanalysis data. We also corrected model surface runoff and SMB for changes in surface elevation by applying the gradient method of Helsen et al. (2012) as described in Calov et al. (2018). The surface runoff R over the ice sheet (SICOPOLIS) is determined as

$$R(x,y,t_{monthly}) = R_{\text{MAR(REAN)}}^{\text{Clim } 1961-1990}(x,y) \quad + \quad (R_{\text{MAR(MIROC)}}(x,y,t_{monthly}) - R_{\text{MAR(MIROC)}}^{\text{Clim } 1961-1990}(x,y))$$

$$+ \left(\frac{\partial R}{\partial z}\right)_{\text{MAR(MIROC)}} (x,y,t) \quad \Delta h_s(x,y,t_{monthly}), \tag{17}$$

where the runoff $R(x,y,t)$ on every grid cell (x,y) at any time t on a monthly time-step was calculated by the climatological mean from 1961-1990 of MAR (forced by reanalysis data) $R_{\text{MAR(rean)}}^{\text{Clim } 1961-1990}(x,y)$ plus the anomaly of the runoff relative to the climatological mean for the same period of time obtained by MAR forced with MIROC5 $(R_{\text{MAR(CMIP5)}}(x,y,t) - R_{\text{MAR(CMIP5)}}^{\text{Clim } 1961-1990}(x,y))$. For ice surface evolving in time $\Delta h_s(x,y,t) = h_s^{\text{obs}}(x,y) - h_s(x,y,t)$, the vertical gradient $\left(\frac{\partial R}{\partial z}\right)_{\text{MAR(MIROC)}} (x,$ determined for every time step, was additionally applied to account for the increase in surface runoff. The observed surface elevation h_s^{obs} of the ice sheet was taken from Bamber et al. (2013). Negative runoff values were set to zero. The correction of runoff for elevation change can be important in some case since, as it was shown in Amundson and Carroll (2018) for tidewater glaciers, large and rapid changes in glacier volume can lead to a high increase in runoff due to surface lowering.

For the present-day condition, the SMB for the glaciers was calculated from relaxation to observed surface elevation h_s^{obs}, with a different relaxation time scale τ for each glacier (see section 4.1):

$$\dot{B} = \frac{h_s^{\text{obs}} - h_s}{\tau} \text{ in m/yr.} \tag{18}$$

With the latter equation we calculated the present-day SMB during the spinup experiment, similarly to Calov et al. (2018). For future scenarios, we added the anomaly of the SMB (relative to the year 2000) to the present-day SMB. The anomaly for each grid cell of the glacier was computed from interpolation of the MAR anomaly of the centerline of the individual glacier and additionally corrected for the glacier elevation change similarly to the surface runoff (Eq. 17), but for the SMB-calculation, Δh_s is the glacier elevation change compared to present-day, assuming that the derived glacier shape from the present-day dataset is for the year 2000.

$$SMB(x,t) = SMB_{\text{MAR(MIROC)}}^{2000}(x) \quad + \quad (SMB_{\text{MAR(MIROC)}}(x,t) - SMB_{\text{MAR(MIROC)}}^{2000}(x))$$

$$+ \left(\frac{\partial SMB}{\partial z}\right)_{\text{MAR(MIROC)}} (x,t) \quad \Delta h_s(x,t), \tag{19}$$

The time series of cumulative SMB (without surface correction) and the annual subglacial discharge for each glacier are shown in the supporting information (Fig. S1 and Fig. S2)

3.4 Fjord temperature and salinity profiles: CTD measurement and Ocean Reanalysis data

Determining vertical temperature and salinity profiles in Greenland fjords, which are the input for the plume model, is a challenging task. Measurements inside Greenland fjords are rare and do not cover all of them. For some fjords, several conductivity-temperature-depth (CTD) measurements exist, but they are mostly infrequent and often not performed close enough to the calving front. It is also important to note that T-S profiles obtained from CTD measurements have to be treated with caution because they represent only a 'time shot' of fjord properties which vary significantly in time (Jackson et al., 2014).

However, the question arises on how to treat fjords, where no CTD measurements are available. A possible solution is to use ocean reanalysis data. Here we use the TOPAZ Arctic Ocean Reanalysis data[2] (Xie et al., 2017) and compare them with existing CTD measurements. Note that for all twelve glaciers used in this study the CTD measurements from the adjacent fjord are available and we use them throughout our experiments as the preferred Temperature-Salinity-profile (TS-profile). To make assumptions on potential impacts of the differences between reanalysis and CTD profiles on the glacier response to climate change we investigate both types of ocean data (reanalysis and measurements). Figure 4 illustrates the strong bias towards colder temperatures for the reanalysis data set. The detailed description on how the temperature profiles were derived from the reanalysis data and illustrations of both temperatures profiles that forced the glacier-plume model can be found in the supporting information.

Thus, for each glacier, we have two temperature profiles (CTD and reanalysis) that are used to simulate the present-day submarine melt rate in the spin-up experiment. We did not consider a seasonal cycle since this would only be represented in the upper surface layer, which is of less importance for the calculation of the submarine melt rate. For future simulations, we prescribed simple scenarios for the ocean temperature anomalies (ΔT) based on minimal and maximal temperature trends simulated by several CMIP5 models (GFDL-ESM2G, MPI-ESM-LR, and HadGEM2-CC). The trend is added uniformly to the entire Temperature profiles (both CTD and reanalysis) for the future simulations.

$$T(Z,t) = T(Z)_{\mathrm{CTD/REAN}} \quad + \quad \Delta T_{\mathrm{min/max}} \cdot t \tag{20}$$

To determine this temperature trend ΔT for each CMIP5 model we used the grid-cell closest to each fjord but with a depth larger than 400m. The temperature trends were approximated by linear regression as illustrated in Fig. 5. The Figure shows also the big discrepancy between the model temperatures and CTD measurement at 700m depth which was the motivation to use 400 m depth only. The temperature trends and cell locations for each glacier and CMIP5 model are listed in Table S1 of the supporting information, while the resulting minimal and maximal temperature trends of these trends for each glacier $\Delta T_{\mathrm{min/max}}$ are listed in Table 1.

---

[2]http://marine.copernicus.eu/services-portfolio/access-to-products/?option=com_csw&view=details&product_id=ARCTIC_REANALYSIS_
PHYS_002_003

4 Experimental setup

4.1 Selection of model parameters and model spin up

Model calibration and spinup for each glacier has been made in two steps. First, the standalone glacier model (without the plume parameterization) was pre-calibrated to best match observed surface elevation, grounding-line position (accuracy $\pm 2\,\text{km}$ has been required) and velocity profile assuming a constant prescribed submarine melt rate. Dynamic parameters E, W_s, A_s and q (equation 2) were varied for this purpose (affecting basal shear stress, lateral stress, and calving front boundary condition), along with the freshwater depth in crevasses d_w and the constant melt rate m, for each glacier separately. The values of dynamic parameters and relaxation time scales for each glacier are listed in the supporting information Table S2.

Once the four dynamic parameters and the relaxation time scale are set in our pre-calibration, we performed a set of spin-up experiments with the coupled glacier-plume model for each glacier. In the spin-up experiments the submarine melt rate is now simulated interactively by the plume model which requires subglacial discharge and temperature and salinity profiles as input-data. We used monthly subglacial discharge for the year 2000 derived from SICOPOLIS (section 3.3). Vertical temperature and salinity profiles in these experiments were taken from the reanalysis data, averaged over the time interval 1990–2010 or from recent CTD data, and were held constant in time (Fig. S3, supporting information). Nonetheless, in the spin-up experiments the submarine melt rate is not constant since changes in the grounding line depth and shape of the floating tongue (if present) affect the submarine melt. We chose the year 2000 as the quasi-equilibrium initial state for "future" climate change simulations since the mass loss of GrIS during the last decade of the 20th century was rather small (ca. 0.1 mm/yr in sea level equivalent) compared to that observed in the first decade of the 21st century (Vaughan et al., 2013).

We generate an ensemble of model realizations by varying two model parameters: freshwater depth in crevasses d_w and the plume linear scaling parameter β (factor in a range from 0.3 to 3 that multiplies the simulated melt rate profile), which control calving rate and submarine melting, respectively. We run the coupled model for each combination of these two parameters over 100 years, so that the glacier at the end of the simulation was close to an equilibrium state and we exclude model versions which simulated the grounding line position more than 2 km distant from the observed one or which displays a low-frequency oscillatory behaviour with advancing glacier front over the last 20 years of simulations. The list of the parameter range and number of valid realizations for CTD and reanalysis data can be found in the supporting information, Tab. S3. The partition between calving and submarine melting was available from Enderlin and Howat (2013) for some glaciers, and was used it as an additional constraint for the model parameter combinations.

4.2 Future climate scenarios

For all future simulations, we used valid combinations of model parameters and corresponding initial conditions obtained at the end of the 100-yrs spin-up runs. The anomalies of SMB were derived from the regional climate model MAR simulations as described in Section 3.3 (Fig. S1, supporting information). To compute future ocean temperature, we use the minimal and maximal ocean temperature trends (Table 1) added on the temperature-depth profiles for each glacier (Section 3.4). We prescribe the subglacial discharge for each glacier off-line with a monthly time step from the output of the ice sheet model

SICOPOLIS. The yearly subglacial meltwater discharge is depicted in Fig. S2. Figure 2 illustrates the data input required for each glacier to simulate their response to future atmospheric and oceanic warming.

All forcing scenarios were applied for the years 2000–2100. In addition, we run the model for 100 years with zero anomalies of temperature, SMB, and subglacial discharge to determine unforced model drift.

To express ice volume loss in sea level rise equivalent we used the multiplication factor l under the assumption of oceans occupying $A_{\mathrm{ocean}} = 360 \cdot 10^6 \ \mathrm{km}^2$:

$$l = \frac{\rho_{\mathrm{ice}}}{\rho_{\mathrm{fw}} A_{\mathrm{ocean}}} \tag{21}$$

leads to a SLR of $2.55 \cdot 10^{-3}$ mm for $1 \ \mathrm{km}^3$ of ice volume V_{SLR} with the density of ice $\rho_{\mathrm{ice}} = 917 \ \mathrm{kg \ m^{-3}}$, and fresh water $\rho_{\mathrm{fw}} = 1000 \ \mathrm{kg \ m^{-3}}$.

The contributing ice volume V_{SLR} is determined by the lost ice volume above flotation from each glacier.

5 Results

5.1 Present-day state

The simulated present-day glacier thickness and velocity profiles for the different submarine melting and calving ratios are depicted in Fig. 6 with a close-up to the grounding line in Fig. S5, supporting information. Note that we allow for small floating termini, since many tidewater glaciers still evolve them on a seasonal scale and glacier fronts are also mostly undercut and thus missing a pure vertical cliff without any floating terminus (Bevan et al., 2012; Straneo et al., 2016; Rignot et al., 2015). Each line in the figure corresponds to a different combination of model parameters β and d_w listed in Tab. S3, supporting information. We found that for some glaciers, the grounding line demonstrates a high sensitivity to the melting/calving ratio, while others are primarily controlled by their bedrock topography and have relatively small variations in their grounding line position over the whole melting/calving ratio range. Upernavik Glacier is an example of the latter case (Fig. S9 and S10, supporting information). In general, we observed higher velocities at the glacier terminus when higher calving rates were applied. Thus, if a glacier is not strongly buttressed by a sill or lateral resistance, different values of velocity at the glacier terminus due to different d_w strongly affect the equilibrium grounding line position. Such behavior points to the crucial role of the bedrock topography for glacier dynamics. The simulated realistic velocity profiles (Fig. 6) for Gade Glacier and Jakobshavn-Isbrae lead to slightly thinner than observed glaciers. For Jakobshavn-Isbrae we were only able to achieve stable states using T-S profiles from the reanalysis dataset, since CTD measurements showed significantly warmer temperatures and the resulting high submarine melt rate led to the retreat of the glacier on the retrograde (upstream deepening) bedrock.

Table 2 provides a comparison of simulations with observational data derived by Enderlin and Howat (2013). Only the glaciers Kong-Oscar and Docker-Smith showed a grounding line flux $\mathrm{Flx}_{\mathrm{gl}}$ matching the observational data. All other glaciers have smaller grounding line fluxes than in Enderlin and Howat (2013). However, it should be noted that many glaciers accelerated since 2000, so it is not clear whether the fluxes reported by Enderlin and Howat (2013) are directly comparable with our equilibrium fluxes. Additionally, Enderlin and Howat (2013) derived submarine melt rates for the floating termini of

the glaciers only since they could not account for melting of vertical glacier fronts due to limitations of their methodological approach. For a direct comparison to Enderlin and Howat (2013), we calculate $\mathrm{MeltFlx}$ of the simulated glaciers by only considering the mass loss from the floating tongue induced by submarine melting. The ratios of submarine melting to grounding line discharge of our simulations lie within the uncertainty ranges determined by Enderlin and Howat (2013). However, these uncertainties are quite large and thus allow broad parameter combinations range for some glaciers. For Jakobshavn, a high calving flux was needed in order to obtain realistic present-day velocity profile for the coupled glacier-plume model (Fig. 6). This results in simulated glacier profiles without any floating terminus ($\mathrm{MeltFlx} = 0$), which is not consistent with Enderlin and Howat (2013). Therefore, this simulated glacier does not match the ratio of submarine melting to grounding line discharge ratio given in Enderlin and Howat (2013) ($\mathrm{MeltFlx}^{\star E}/\mathrm{Flx}_{gl}^{\star E}$ Table 2). The high calving flux required to obtain the precise grounding line position might result from an error in bedrock data or a problem with the flux-weighted averaging. The simulated Daugaard-Jensen Glacier only has a stable position with submarine melt rates lower than in Enderlin and Howat (2013).

5.2 Future simulations

After obtaining the present-day state (year 2000), we then ran the model ensemble with all valid combinations of the parameters β and d_w for 100 simulation years, applying MAR SMB anomalies, monthly subglacial discharge and two scenarios for ocean temperature change (minimum and maximum) as forcing. All results shown here have a small model drift subtracted from the calculated values, to ensure that the simulated SLR is a response to the climate change signal. The glaciers' response to climate change strongly depends on the combination of model parameters and scenarios, resulting in high uncertainty ranges. The simulations that led to a median-range[3] SLR for each glacier are depicted in Figure 7. After 100 years, some glaciers retreat entirely and become land-terminating (Alison, Daugaard-Jensen, Kangerlussuaq, Store), while others barely show a change in the position of the grounding line (Helheim). The individual contribution of each glacier to SLR for the median-range[3] SLR experiments is shown in Fig. 8 a. Jakobshavn-Isbrae shows the most significant contribution to SLR, due to the big catchment area and large retreat, followed by Kangerlussuaq Glacier due to its full retreat.

When forced by comprehensive climate change scenarios (changes in SMB with the surface elevation feedback, ocean temperature T and subglacial discharge Q) the median estimate for SLR contribution from all 12 glaciers is about 18 mm (17.9 mm) at the year 2100 (Fig. 8 a, and Fig. 8 b, blue curve). To quantify the role of the individual forcing factors, we performed an additional set of simulations with the same model versions corresponding to the median SLR response (18mm) but applying the three different forcing factors in sequence. With the same model version we rerun for each glacier the experiment omitting changes in subglacial discharge (denoted "SMB + T" in Fig. 8 b, pink curve) and omitting changes in subglacial discharge and ocean temperatures (denoted "SMB" in Fig. 8 b, sum of the brown, orange and yellow areas). The total effect of SMB change on SLR is decomposed into "static" (brown), "dynamic" (yellow) and "dynamic effect with elevation correction" (orange). "Static" effect was computed as the cumulative integral of SMB anomalies over the fixed present-day catchment and elevation of individual glaciers. As Fig. 8 b shows, this component is close to zero which is explained by the geometry of the glaciers'

---

[3]median for an odd number of simulations, the first value of higher half for an even number of simulation

catchment area, where the ablation area is much smaller than accumulation area. For some glaciers, the cumulative SMB over the glacier's catchment even increased towards the end of 21 century due to increased precipitation over accumulation area (Fig S1, supporting information). The SMB forcing used to force the glacier model comes from the original MAR output data (Fig. 2), in which no surface-elevation feedback is considered since the ice-sheet surface is considered constant over time.

5 In the "dynamic" (yellow) experiment we force the glacier model with the original MAR output-data (no surface-elevation feedback). Thus most of SLR due to SMB change alone occurs through the dynamical processes – thinning and acceleration of glaciers, which in turn affects the calving rate and grounding line retreat. In the third experiment (orange) we consider the surface-elevation feedback by correcting the SMB-forcing for the elevation change on every time step (eq. 19). The resulting additional SLR (Fig. 8 b, orange) is negligible compared to the dynamic response (yellow curve). Thus, the surface elevation

10 feedback has only a minor effect on the glaciers response to SMB change which is not the case for the entire GrIS (Calov et al., 2018) where this effect is important. As explained above, we attribute 30 % of the 18 mm SLR to the response to changes in SMB alone. The remaining 70 % of SLR is thus caused by the response to ocean warming and increased subglacial discharge (Fig. 8 b, blue and pink area together). We found that both factors, ocean warming and increased subglacial discharge, are of comparable importance for SLR (by comparing the blue and pink curve in Fig. 8 b These estimates are valid only for

15 the cumulative SLR of all 12 glaciers. Each individual glacier may respond differently to the individual forcing factors. For instance, Kong-Oscar Glacier (Fig. 9) is slightly gaining mass with the SMB forcing alone and shows a retreat by 10 km and a contribution of 1 mm to SLR due to ocean warming. When the increase in subglacial discharge is added to the ocean warming, the glacier retreats another 10 km and contributes additionally 2 mm to SLR. At the same time, Yngvar-Nielson Glacier (Fig. 10) is already retreating significantly in the experiment with the SMB forcing alone. Ocean warming and increased subglacial

20 discharge also contribute to SLR, but for Yngvar-Nielson the largest SLR contributor is the SMB change. The different dynamic responses of glaciers can be clearly seen for Rink-Isbrae Glacier and Store Glacier: Both have approximately the same SMB forcing (Fig. S1) but the unstable position of Store Glacier (on the tip of a steep sill, Fig. 6) causes the glacier to be more vulnerable to mass changes at the glacier terminus and when pushed to the retrograde bed the glacier automatically retreats and thus contributes to additional SLR. The dynamic response leads to a significant higher SLR for Store Glacier than for Rink

25 Glacier.

Above we discussed only median-range scenarios, but the uncertainty ranges are crucial when projecting future SLR. Therefore, Fig. 11 shows the first and third quartile together with the median values of the individual glacier's contributions to SLR for all sets of valid model realisations and full forcing (SMB + T (max/min) + Q) against the simulated present-day glacier discharge. Their potential SLR and grounding line retreat are listed in Table 3 and 4. Figure 11 shows a correlation between present-day

30 grounding line discharge and the contribution to future SLR for individual glaciers. Jakobshavn and Kong-Oscar show the largest spread.

The only 'uncertainty' in the ocean forcing is contained in the choice of the ocean temperature trend ($T_{\min}$ or $T_{\max}$). Thus, to analyse whether the uncertainty ranges in SLR result primarily from the uncertainty range in the forcing or from the uncertainties of the model parameters/ the melting-to-calving proportion (uncertainty ranges in β and d_w) we show in Fig.

35 12 results of experiments forced only by $T_{\min}$ or $T_{\max}$ ocean warming scenarios. Figure 12 shows a small future SLR and

uncertainty range related to glaciers responding to stand-alone SMB forcing (except for Jakobshavn-Isbrae). Since the SMB forcing is the same in all simulations, the spread originates from the differences in initial states cause by different d_w and β combinations, thus different melting-to-calving proportion.

For Kong-Oscar Glacier, the negative SLR originates from the increase in SMB in this region under the RCP 8.5 scenario (Fig. S1). Including the forcing factors of submarine melt, T and Q, leads to a relatively high SLR contribution and high SLR uncertainty ranges for the Kong-Oscar, Kangerlussuaq, Rink, and Daugaard-Jensen glacier (Fig. 12 shown by the blue columns). Since these high uncertainties arise also with the same forcing (only $T_{\min}$ or $T_{\max}$), we attribute the major source of uncertainty to the different combinations of the model parameters d_w and β. For each experiment, we also investigated whether the choice of using CTD measurements or reanalysis data for the initial ocean temperature profile had an impact on the potential SLR (Fig. S11, supporting information). If we neglect Jakobshavn and Kong Oscar glacier (no valid simulations with CTD profiles available), only Helheim glacier showed a stronger increase in SLR when reanalysis data were used to construct T-S profiles. For the rest of the glaciers the choice of using reanalysis data or CTD data for T-S profiles shows only minor differences in SLR.

To approximate the total contribution of SLR of all glaciers we aim to upscale the results derived by the representative 12 glaciers, studied here. Thus, in spite of these uncertainties, we use the median scenarios from Fig. 11 to estimate the relationship between present-day glacial discharge and contribution to SLR for the year 2100 by fitting a linear regression determined with the least square method. The derived slope ($0.12 \, \mathrm{mm \, km^{-3} \, a}$) is statistically significant (p-values < 0.01) and has a correlation coefficient of 0.74. With this slope and the total flux of all outlet glaciers ($\sim 450 \, \mathrm{Gt/a}$ (Enderlin et al., 2014; Rignot et al., 2008)), the simple linear relationship would imply a total SLR contribution of roughly 5 cm (54 mm) from all Greenland outlet glaciers at the year 2100. This upscaling method is very sensitive to the choice and amount of glaciers as Fig. 13 shows. When choosing only four glaciers (as in Nick et al. (2013)) to determine the slope of the regression line, the slope can range between $0.03 - 0.16 \, \mathrm{mm \, km^{-3} \, a}$ (by picking the four glaciers that led to the most extreme cases, Fig.13). This leads to an uncertainty range of roughly 15–80 mm, overlapping with the higher uncertainty range of Nick et al. (2013)(65-183mm). Due to the low sample size of four glaciers, these resulting regression line is however not statistically significant in the case for the smaller slope of (0.03). Nonetheless, the experiment underlines the importance of choosing a sufficiently large sample size and representative types of glaciers.

6 Discussion and Conclusions

For 12 selected outlet glaciers of the GrIS, we investigated their potential contribution to SLR during the 21st century for the RCP 8.5 scenario. To study the role of future changes in SMB, ocean temperature and subglacial discharge, we used a 1D flowline model which includes a surface crevasse calving law and is coupled to the 1D line plume model of Jenkins (2011). In our model, the calving flux can be altered by choosing a parameter for the freshwater depth in crevasses, and the submarine melt rate can be changed by a scaling factor. We also used two different initial temperature-salinity profiles – one derived

from reanalysis data and another from in-situ measurements inside the fjords. For the present-day simulations, we varied the submarine melting and the calving parameter to obtain a glacier profile similar to observations. For all outlet glaciers, we were able to achieve a reasonable agreement between the simulated and observed present-day profiles. However, for the Jakobshavn Isbrae glacier, the simulated submarine melt and grounding line discharge ratio does not agree with that derived by Enderlin and Howat (2013), as this ice stream could not develop a floating terminus in our simulations. The melt ratio derived by Enderlin and Howat (2013) could also not be achieved for Daugaard-Jensen.

In order to simulate the future glacial contribution to SLR under the RCP 8.5 scenario, we prescribed changes in SMB and subglacial discharge based on results of the regional climate model MAR. Anomalies of ocean temperatures from CMIP5 climate models were used to generate minimum and maximum scenarios for the ocean temperature change until year 2100. Simulated SLR contributions for the year 2100 compare well to values from Nick et al. (2013) for Jakobshavn Isbrae. The conservative estimates of Jakobshavn Isbrae contribution to SLR obtained with the 3D model of Bondzio et al. (2017) also lie within our uncertainty range. For Kangerlussuaq Glacier our estimates of SLR contribution exceed the estimates of Nick et al. by 2 mm, while for Helheim Glacier our SLR estimates are below the estimates of Nick et al. (2013). In our simulations all glaciers experience a grounding line retreat which is found as well by Nick et al. (2013) but was not simulated by Peano et al. (2017). This discrepancy might be related to the coarse spatial resolution (5 km) of Peano et al. (2017) model (especially for the deep and narrow trough in Jakbobshavn) or processes upstream of the glacier might have counterbalanced the glacier retreat, which we could not simulate with a 1D flowline model. The difference to Nick et al. (2013) can be explained by their different treatment of calving processes (in their model freshwater depth in the crevasses was linked to runoff) or submarine melting (Nick et al. (2013) did not account for the influence of changing subglacial discharge). Also, Nick et al. (2013) used the surface elevation and velocity profile from the center line. For Helheim glacier and Kangerlussuaq glacier they took the width of the whole catchment area whereas at Jakobshavn Isbrae the width was constrained to the width of the trough and a constant lateral flux was added to gain the high grounding line flux of Jakobshavn Isbrae. By contrast, we used a flux-weighted average of the whole glacier catchment area to represent each individual glacier.

We also investigated how different forcing factors influence the simulated future SLR. For the ensemble of the 12 glaciers, SLR was over threefold larger when the changes in subglacial discharge and ocean temperature were added to changes in SMB. This underlines the critical role of submarine melting for future GrIS contribution to SLR. Moreover, we found significantly larger SLR when the subglacial discharge is allowed to increase in the scenarios. In fact, the amount of SLR attributed to subglacial discharge is similar to the SLR attributed to an increased ocean temperature. Thus, for future projections, both factors affecting submarine melt rate – subglacial discharge and ocean temperature – need to be taken into account. Also we show that even the almost negligible (compared to SLR) SMB-forcing results in a considerable contribution to SLR due to the dynamical response of the glaciers. This response, however is strongly controlled by the underlying bed topography of each individual glacier (e.g. Rink-Isbrae and Store Glacier). It should also be noted that our 1D flowline model is based on a crevasse depth calving law and thus does not account for undercut calving or buoyancy-driven calving (Benn et al., 2017), which in turn is strongly influenced by submarine melting. This mechanism might act as a further amplifier of glacial mass loss that is not accounted for in our results.

Our experiments also reveal large uncertainty ranges, primarily attributed to the different combinations of the two model parameters that determine submarine melting and calving fluxes. Nonetheless, the simulated melt/calving ratios lie within the uncertainty range of observations, and reducing the uncertainties with more precise observational data would probably improve future simulations. On the other hand, our results are not significantly affected by the choice of CTD or reanalysis data when defining the initial ocean temperature and salinity profiles. This suggests that accurate process-based models and observational constraints on submarine melt and calving are more important when making projections about the future response of Greenland outlet glaciers to climate change. Additional uncertainty related to dynamic parameters and topography data (bedrock, width) are not included in this study.

Overall, we obtain a total Greenland glaciers SLR contribution of approximately 50 mm when assuming a linear relationship between the glacier's present-day grounding line discharge and their contribution to future SLR. Our estimate for SLR is lower than in Nick et al. (2013) (65-183 mm) partly due to the fact that we took into consideration also smaller marine terminating glaciers. As Goelzer et al. (2013) argues, these glaciers probably become land-terminating faster than glaciers with a large grounding line discharge and have less mass influenced by ice-ocean interaction. Therefore our upscaling method for the strong climate change scenario should not be used past the year 2100. Furthermore, we demonstrate the sensitivity of the upscaling method to the choice and number of glaciers: by using only 4 glaciers as in Nick et al. (2013), the different choice of glaciers leads to uncertainty ranges of 15-80mm SLR.

Our simulations considered a constant catchment area for each glacier and did not account for potential changes in lateral inflow from the ice sheet interior. Such increased mass inflow could result in a smaller grounding line retreat but an increased inflow would also result in a broadening of the catchment area, as Goelzer et al. (2013) indicate, which could increase ice sheet mass loss further upstream. The full impact can only be assessed with experiments in which outlet glaciers and the parent ice sheet are fully coupled. Additionally, the 1D flowline model treats lateral processes in a simplified manner, so that more complex bedrock geometries (e.g. branching of glaciers, individual sills, unsymmetrical valley forms) are poorly represented in these estimates. For a first approximation, though, we treat the SLR of 5 cm as additional to that simulated with coarse resolution GrIS ice-sheet models, since the cumulative SMB forcing (without glacier response) over the glaciers' area is negligible. Some inconsistency arises from the fact that the database used to initialize the glaciers at the year 2000 is actually based on the measurements made in 2008/2009, but the total contribution of GrIS to global seal level rise during the first 8 years of the 21st century was only about 3 mm and glaciers contributed not more than half of that. Thus this inconsistency has only a minor effect on our moderate approximation of 50 mm.

By adding the 5 cm contribution of outlet glaciers to the 8.8 cm (mid-range scenario) simulated by Calov et al. (2018) for the year 2100 using an ice sheet model under the same climate scenario, we arrive at a total GrIS contribution 138 mm (103 -168 mm from lower sample size range).

This implies that the dynamical response of Greenland's outlet glaciers to climate change can increase GrIS contribution to SLR in 2100 by over 50 %.

Author contributions. J.B designed the study together with A. G.. M.P. wrote the glacier model in FORTRAN and provided 1D topography data for the 12 glaciers of this study. J.B. coupled the numerical plume model to the glacier model, and implemented the surface-correction method. Together with S.B, R.C and M.W, J.B. created the projected subglacial discharge and surface-mass balance data set for each glacier respectively. J.B. carried out the experiments, created the figures and wrote the manuscript, supported by all co-authors.

5   *Competing interests.* The authors declare no competing interests.

Acknowledgements. This work was funded by Leibniz-Gemeinschaft, WGL Pakt für Forschung SAW-2014-PIK-1. M. W. and R. C. acknowledge support by the BMBF funded project PalMod.

References

Amundson, J. M. and Carroll, D.: Effect of Topography on Subglacial Discharge and Submarine Melting During Tidewater Glacier Retreat, Journal of Geophysical Research: Earth Surface, 123, 66–79, https://doi.org/10.1002/2017JF004376, http://doi.wiley.com/10.1002/2017JF004376, 2018.

5 Aschwanden, A., Fahnestock, M. A., and Truffer, M.: Complex Greenland outlet glacier flow captured, Nature Communications, 7, 10 524, 2016.

Bamber, J. L., Griggs, J. a., Hurkmans, R. T. W. L., Dowdeswell, J. a., Gogineni, S. P., Howat, I., Mouginot, J., Paden, J., Palmer, S., Rignot, E., and Steinhage, D.: A new bed elevation dataset for Greenland, Cryosphere, 7, 499–510, https://doi.org/10.5194/tc-7-499-2013, 2013.

Beckmann, J., Perrette, M., and Ganopolski, A.: Simple models for the simulation of submarine melt for a Greenland glacial system model, Cryosphere, 12, 301–323, https://doi.org/10.5194/tc-12-301-2018, 2018.

10 Benn, D. I., Aström, J., Zwinger, T., Todd, J., Nick, F. M., Cook, S., Hulton, N. R., and Luckman, A.: Melt-under-cutting and buoyancy-driven calving from tidewater glaciers: New insights from discrete element and continuum model simulations, Journal of Glaciology, 63, 691–702, https://doi.org/10.1017/jog.2017.41, 2017.

Bevan, S. L., Luckman, a. J., and Murray, T.: Glacier dynamics over the last quarter of a century at Helheim, Kangerdlugssuaq and 14 other major Greenland outlet glaciers, The Cryosphere, 6, 923–937, https://doi.org/10.5194/tc-6-923-2012, http://www.the-cryosphere.net/6/923/2012/, 2012.

Bondzio, J. H., Morlighem, M., Seroussi, H., Kleiner, T., Rückamp, M., Mouginot, J., Moon, T., Larour, E. Y., and Humbert, A.: The mechanisms behind Jakobshavn Isbræ's acceleration and mass loss: A 3-D thermomechanical model study, Geophysical Research Letters, 44, 6252–6260, https://doi.org/10.1002/2017GL073309, 2017.

20 Calov, R., Beyer, S., Greve, R., Beckmann, J., Willeit, M., Kleiner, T., Rückamp, M., Humbert, A., and Ganopolski, A.: Simulation of the future sea level contribution of Greenland with a new glacial system model, The Cryosphere Discussions, 2018, 1–37, https://doi.org/10.5194/tc-2018-23, https://www.the-cryosphere-discuss.net/tc-2018-23/, 2018.

Carroll, D., Sutherland, D. a., Shroyer, E. L., Nash, J. D., Catania, G. a., and Stearns, L. a.: Modeling Turbulent Subglacial Meltwater Plumes: Implications for Fjord-Scale Buoyancy-Driven Circulation, Journal of Physical Oceanography, p. In press, https://doi.org/10.1175/JPO-D-15-0033.1, http://journals.ametsoc.org/doi/abs/10.1175/JPO-D-15-0033.1, 2015.

Chen, X., Zhang, X., Church, J. A., Watson, C. S., King, M. A., Monselesan, D., Legresy, B., and Harig, C.: The increasing rate of global mean sea-level rise during 1993-2014, Nature Climate Change, 7, 492–495, https://doi.org/10.1038/nclimate3325, http://dx.doi.org/10.1038/nclimate3325{%}0Ahttp://10.0.4.14/nclimate3325{%}0Ahttp://www.nature.com/nclimate/journal/vaop/ncurrent/abs/nclimate3325.html{#}supplementary-information{%}5Cnhttp://www.nature.com/doifinder/10.1038/nclimate3325, 2017.

30 Cowton, T., Slater, D., Sole, A., Goldberg, D., and Nienow, P.: Modeling the impact of glacial runoff on fjord circulation and submarine melt rate using a new subgrid-scale parameterization for glacial plumes, Journal of Geophysical Research: Oceans, 120, 796–812, https://doi.org/10.1002/2014JC010324, 2015.

Dowdeswell, J. A., Evans, J., and Cofaigh, C. Ó.: Submarine landforms and shallow acoustic stratigraphy of a 400 km-long fjord-shelf-slope transect, Kangerlussuaq margin, East Greenland, Quaternary Science Reviews, 29, 3359–3369, https://doi.org/10.1016/j.quascirev.2010.06.006, http://dx.doi.org/10.1016/j.quascirev.2010.06.006, 2010.

Enderlin, E. M. and Howat, I. M.: Submarine melt rate estimates for floating termini of Greenland outlet glaciers (2000â2010), Journal of Glaciology, 59, 67–75, https://doi.org/10.3189/2013JoG12J049, http://openurl.ingenta.com/content/xref?genre=article{&}issn=0022-1430{&}volume=59{&}issue=213{&}spage=67, 2013.

Enderlin, E. M., Howat, I. M., and Vieli, A.: High sensitivity of tidewater outlet glacier dynamics to shape, The Cryosphere, 7, 1007–1015, https://doi.org/10.5194/tc-7-1007-2013, http://www.the-cryosphere.net/7/1007/2013/, 2013.

Enderlin, E. M., Howat, I. M., Jeong, S., Noh, M. J., Van Angelen, J. H., and Van Den Broeke, M. R.: An improved mass budget for the Greenland ice sheet, Geophysical Research Letters, 41, 866–872, https://doi.org/10.1002/2013GL059010, 2014.

Fettweis, X., Franco, B., Tedesco, M., Van Angelen, J. H., Lenaerts, J. T., Van Den Broeke, M. R., and Gallée, H.: Estimating the Greenland ice sheet surface mass balance contribution to future sea level rise using the regional atmospheric climate model MAR, Cryosphere, 7, 469–489, https://doi.org/10.5194/tc-7-469-2013, 2013.

Fried, M. J., Catania, G. A., Bartholomaus, T. C., Duncan, D., Davis, M., Stearns, L. A., Nash, J., Shroyer, E., and Sutherland, D.: Distributed subglacial discharge drives significant submarine melt at a Greenland tidewater glacier, pp. 4–7, 2015.

Fürst, J. J., Goelzer, H., and Huybrechts, P.: Ice-dynamic projections of the Greenland ice sheet in response to atmospheric and oceanic warming, The Cryosphere, 9, 1039–1062, https://doi.org/10.5194/tcd-8-3851-2014, http://www.the-cryosphere-discuss.net/8/3851/2014/, 2015.

Gillet-Chaulet, F., Gagliardini, O., Seddik, H., Nodet, M., Durand, G., Ritz, C., Zwinger, T., Greve, R., and Vaughan, D. G.: Greenland ice sheet contribution to sea-level rise from a new-generation ice-sheet model, Cryosphere, 6, 1561–1576, https://doi.org/10.5194/tc-6-1561-2012, 2012.

Goelzer, H., Huybrechts, P., Fürst, J., Nick, F., Andersen, M., Edwards, T., Fettweis, X., a.J. Payne, and Shannon, S.: Sensitivity of Greenland ice sheet projections to model formulations, Journal of Glaciology, 59, 733–749, https://doi.org/10.3189/2013JoG12J182, http://www.igsoc.org/journal/59/216/j12J182.html, 2013.

Goelzer, H., Robinson, A., Seroussi, H., and van de Wal, R. S.: Recent Progress in Greenland Ice Sheet Modelling, Current Climate Change Reports, 3, 291–302, https://doi.org/10.1007/s40641-017-0073-y, http://link.springer.com/10.1007/s40641-017-0073-y, 2017.

Helsen, M. M., van de Wal, R. S. W., van den Broeke, M. R., van de Berg, W. J., and Oerlemans, J.: Coupling of climate models and ice sheet models by surface mass balance gradients: application to the {Greenland} Ice Sheet, The Cryosphere, 6, 255–272, https://doi.org/doi:10.5194/tc-6-255-2012, 2012, 2012.

Jackson, R. H., Straneo, F., and Sutherland, D. A.: Externally forced fluctuations in ocean temperature at Greenland glaciers in non-summer months, Nature Geoscience, 7, 503–508, https://doi.org/10.1038/ngeo2186, http://www.nature.com/ngeo/journal/v7/n7/full/ngeo2186.html?WT.ec{_}id=NGEO-201407, 2014.

Jackson, R. H., Shroyer, E. L., Nash, J. D., Sutherland, D. A., Carroll, D., Fried, M. J., Catania, G. A., Bartholomaus, T. C., and Stearns, L. A.: Near-glacier surveying of a subglacial discharge plume: implications for plume parameterizations, Geophysical Research Letters, https://doi.org/10.1002/2017GL073602, http://doi.wiley.com/10.1002/2017GL073602, 2017.

Jenkins, A.: Convection-Driven Melting near the Grounding Lines of Ice Shelves and Tidewater Glaciers, Journal of Physical Oceanography, 41, 2279–2294, https://doi.org/10.1175/JPO-D-11-03.1, http://journals.ametsoc.org/doi/abs/10.1175/JPO-D-11-03.1, 2011.

Khan, S. a., Kjaer, K. H., Bevis, M., Bamber, J. L., Wahr, J., Kjeldsen, K. K., Bjork, A. a., Korsgaard, N. J., Stearns, L. a., van den Broeke, M. R., Liu, L., Larsen, N. K., and Muresan, I. S.: Sustained mass loss of the northeast Greenland ice sheet triggered by regional warming, Nature Clim. Change, 4, 292–299, https://doi.org/10.1038/nclimate2161, http://dx.doi.org/10.1038/nclimate2161{%}5Cn10.1038/nclimate2161{%}5Cnhttp://www.nature.com/nclimate/journal/v4/n4/abs/nclimate2161.html{#}supplementary-information, 2014.

Lindbäck, K., Pettersson, R., Hubbard, A. L., Doyle, S. H., Van As, D., Mikkelsen, A. B., and Fitzpatrick, A. A.: Sub-glacial water drainage, storage, and piracy beneath the Greenland ice sheet, Geophysical Research Letters, 42, 7606–7614, https://doi.org/10.1002/2015GL065393, 2015.

Moon, T., Joughin, I., Smith, B., and Howat, I.: 21st-Century Evolution of Greenland Outlet Glacier Velocities, Science, 336, 576–578, 2012.

5 Morlighem, M., Rignot, E., Mouginot, J., Seroussi, H., and Larour, E.: Deeply incised submarine glacial valleys beneath the Greenland ice sheet, Nature Geoscience, 7, 418–422, https://doi.org/10.1038/ngeo2167, http://www.nature.com/doifinder/10.1038/ngeo2167, 2014.

Mortensen, J., Bendtsen, J., Motyka, R. J., Lennert, K., Truffer, M., Fahnestock, M., and Rysgaard, S.: On the seasonal freshwater stratifi-cation in the proximity of fast-flowing tidewater outlet glaciers in a sub-Arctic sill fjord, Journal of Geophysical Research: Oceans, 118, 1382–1395, https://doi.org/10.1002/jgrc.20134, 2013.

10 Muresan, I. S. and Khan, S. A.: Modelling dynamics of Jakobshavn Isbr{æ} and its contribution to sea level rise over the past and future century, Danmarks Tekniske Universitet (DTU), 2016.

Nick, F., van der Veen, C., Vieli, a., and Benn, D.: A physically based calving model applied to marine outlet glaciers and implications for the glacier dynamics, Journal of Glaciology, 56, 781–794, https://doi.org/10.3189/002214310794457344, http://openurl.ingenta.com/content/xref?genre=article{&}issn=0022-1430{&}volume=56{&}issue=199{&}spage=781, 2010.

15 Nick, F. M., Vieli, A., Andersen, M. L., Joughin, I., Payne, A., Edwards, T. L., Pattyn, F., and van de Wal, R. S. W.: Future sea-level rise from Greenland's main outlet glaciers in a warming climate, Nature, 497, 235–238, https://doi.org/10.1038/nature12068, http://www.nature.com/doifinder/10.1038/nature12068, 2013.

Peano, D., Colleoni, F., Quiquet, A., and Masina, S.: Ice flux evolution in fast flowing areas of the {Greenland} ice sheet over the 20th and 21st centuries, J. Glaciol., 63, 499–513, https://doi.org/10.1017/jog.2017.12, 2017.

20 Rignot, E. and Mouginot, J.: Ice flow in Greenland for the International Polar Year 2008-2009, Geophys. Res. Lett., 39, L11 501, https://doi.org/10.1029/2012GL051634, 2012.

Rignot, E., Box, J. E., Burgess, E., and Hanna, E.: Mass balance of the {Greenland} ice sheet from 1958 to 2007, Geophys. Res. Lett., 35, L20 502, https://doi.org/10.1029/2008GL035417, 2008.

Rignot, E., Fenty, I., Xu, Y., Cai, C., and Kemp, C.: Undercutting of marine-terminating glaciers in West Greenland, Geophysical Research

25 Letters, 42, 5909–5917, https://doi.org/10.1002/2015GL064236, 2015.

Rignot, E., Fenty, I., Xu, Y., Cai, C., Velicogna, I., Cofaigh, C., Dowdeswell, J. A., Weinrebe, W., Catania, G., and Duncan, D.: Bathymetry data reveal glaciers vulnerable to ice-ocean interaction in Uummannaq and Vaigat glacial fjords, west Greenland, Geophysical Research Letters, 43, 2667–2674, https://doi.org/10.1002/2016GL067832, 2016.

Schaffer, J., Timmermann, R., Erik Arndt, J., Savstrup Kristensen, S., Mayer, C., Morlighem, M., and Steinhage, D.: A global,

30 high-resolution data set of ice sheet topography, cavity geometry, and ocean bathymetry, Earth System Science Data, 8, 543–557, https://doi.org/10.5194/essd-8-543-2016, 2016.

Schoof, C., Davis, A. D., and Popa, T. V.: Boundary layer models for calving marine outlet glaciers, Cryosphere, 11, 2283–2303, https://doi.org/10.5194/tc-11-2283-2017, 2017.

Sciascia, R., Straneo, F., Cenedese, C., and Heimbach, P.: Seasonal variability of submarine melt rate and circulation in an East Greenland

35 fjord, Journal of Geophysical Research: Oceans, 118, 2492–2506, https://doi.org/10.1002/jgrc.20142, http://doi.wiley.com/10.1002/jgrc.20142, 2013.

Seddik, H., Greve, R., Zwinger, T., Gillet-Chaulet, F., and Gagliardini, O.: Simulations of the Greenland ice sheet 100 years into the future with the full Stokes model Elmer/Ice, Journal of Glaciology, 58, 427–440, https://doi.org/10.3189/2012JoG11J177, http://www.igsoc.org/journal/58/209/t11J177.html, 2012.

Slater, D., Nienow, P., Sole, A., Cowton, T. O. M., Mottram, R., Langen, P., and Mair, D.: Spatially distributed runoff at the grounding line of a large Greenlandic tidewater glacier inferred from plume modelling, Journal of Glaciology, pp. 1–15, https://doi.org/10.1017/jog.2016.139, 2017.

Slater, D. A. and Straneo, F.: Localized Plumes Drive Front-Wide Ocean Melting of A Greenlandic Tidewater Glacier, pp. 350–358, https://doi.org/10.1029/2018GL080763, 2018.

Slater, D. A., Nienow, P. W., Cowton, T. R., Goldberg, D. N., and Sole, A. J.: Effect of near-terminus subglacial hydrology on tidewater glacier submarine melt rates, Geophysical Research Letters, 42, 2861–2868, https://doi.org/10.1002/2014GL062494, 2015.

Straneo, F. and Heimbach, P.: North Atlantic warming and the retreat of Greenland's outlet glaciers., Nature, 504, 36–43, https://doi.org/10.1038/nature12854, http://www.ncbi.nlm.nih.gov/pubmed/24305146, 2013.

Straneo, F., Hamilton, G. S., Stearns, L. A., and Society, T. O.: Oceanography 29(4):34â45,, 2016.

Syvitski, J., Andrews, J., and Dowdeswell, J.: Sediment deposition in an iceberg-dominated glacimarine environment, East Greenland: basin fill implications, Global and Planetary Change, 12, 251–270, https://doi.org/10.1016/0921-8181(95)00023-2, 1996.

Vallot, D., Åström, J., Zwinger, T., Pettersson, R., Everett, A., Benn, D. I., Luckman, A., Van Pelt, W. J., Nick, F., and Kohler, J.: Effects of undercutting and sliding on calving: A global approach applied to Kronebreen, Svalbard, Cryosphere, 12, 609–625, https://doi.org/10.5194/tc-12-609-2018, 2018.

van den Broeke, M., Box, J., Fettweis, X., Hanna, E., Noël, B., Tedesco, M., van As, D., van de Berg, W. J., and van Kampenhout, L.: Greenland Ice Sheet Surface Mass Loss: Recent Developments in Observation and Modeling, Current Climate Change Reports, 3, 345–356, https://doi.org/10.1007/s40641-017-0084-8, http://link.springer.com/10.1007/s40641-017-0084-8, 2017.

Van Den Broeke, M. R., Enderlin, E. M., Howat, I. M., Kuipers Munneke, P., Noël, B. P., Jan Van De Berg, W., Van Meijgaard, E., and Wouters, B.: On the recent contribution of the Greenland ice sheet to sea level change, Cryosphere, 10, 1933–1946, https://doi.org/10.5194/tc-10-1933-2016, 2016.

Van Der Veen, C. J. and Whillans, I. M.: Model experixnents on the evolution and stability of ice streams, Annals of Glaciology, 23, 129–137, 1996.

Vaughan, D. G., Comiso, J. C., Allison, I., Carrasco, J., Kaser, G., Kwok, R., Mote, P., Murray, T., Paul, F., Ren, J., Rignot, E., Solomina, O., Steffen, K., and Zhang, T.: Observations: Cryosphere, Climate Change 2013: The Physical Science Basis. Contribution of Working Group I to the Fifth Assessment Report of the Intergovernmental Panel on Climate Change, pp. 317–382, https://doi.org/10.1017/CBO9781107415324.012, 2013.

Xie, J., Bertino, L., Knut, L., and Sakov, P.: Quality assessment of the TOPAZ4 reanalysis in the Arctic over the period 1991-2013, Ocean Science, 13, 123–144, https://doi.org/10.5194/os-13-123-2017, 2017.

Xu, Y., Rignot, E., Fenty, I., Menemenlis, D., and Flexas, M. M.: Subaqueous melting of Store Glacier, west Greenland from three-dimensional, high-resolution numerical modeling and ocean observations, Geophysical Research Letters, 40, 4648–4653, https://doi.org/10.1002/grl.50825, http://doi.wiley.com/10.1002/grl.50825, 2013.
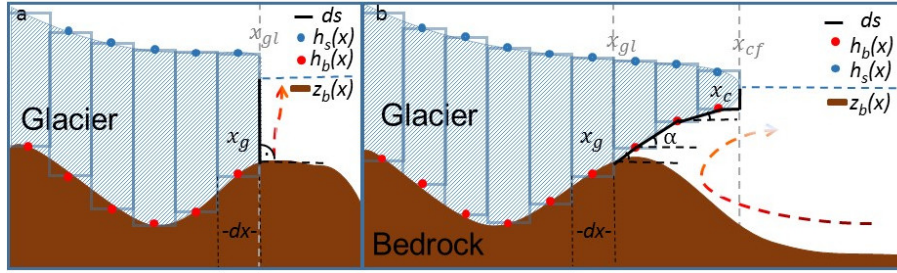
Figure 1. Visualiszation of the 1D glacier model with the staggered grid for a) a tidewater glacier and b) a glacier with a floating tongue. Red dots indicate where the depth of glacier base h_b is defined and blue dots where surface elevation h_s of the glacier is defined. They are calculated at dx/2 - the half width of each grid cell. Last grounded cell has the coordinate x_g and last floating cell has the coordinate x_c. The grounding line x_{gl} is determined at the border of the last grounded cell, where the flotation criterion is not yet achieved. After the grounding line, the calculation of submarine melt along the distance ds (thick, black line) is performed with the line plume model. For a floating tongue (b) every grid cell may have a different angle for the slope of glacial base while for a tidewater glacier (a) the angle is set to 90 degrees. The bedrock elevation z_b (brown, thick line) is equal to h_b for the grounded part and is deeper for the floating part of the glacier.
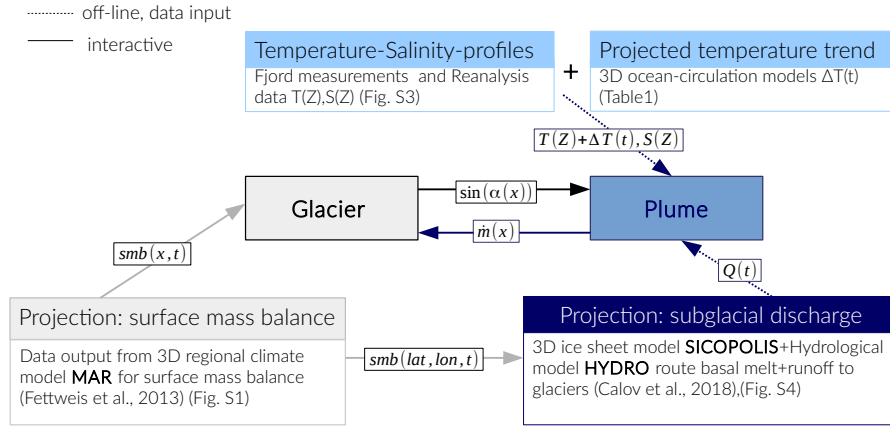
Figure 2. Visualisation of the experimental setup. In the center the coupled glacier-plume model exchange information on the glacier geometry ($\sin(\alpha)$) and the calculated submarine melt rate ($\dot{m}$) on every time step for every glacier grid-point x. To force the coupled model for global warming (RCP 8.5) changes in SMB ($smb(x,t)$), ocean temperature($T(Z) + \Delta T(t)$) and subglacial discharge ($Q(t)$) are considered via data-input. While the SMB changes act on the glacier part, the changes in subglacial discharge and ocean temperature are used to recalculate the submarine melt rate by the plume part of the model. The future evolution of subglacial discharge and ocean temperature is prescribed firmly in the data sets (off-line) that force the plume part, whereas changes in SMB are corrected for the surface elevation feedback and therefore regard changes in the ice surface height interactively. SMB is derived from MAR data (Fettweis et al., 2013), also used to derive the subglacial discharge for each glacier by Calov et al. (2018).
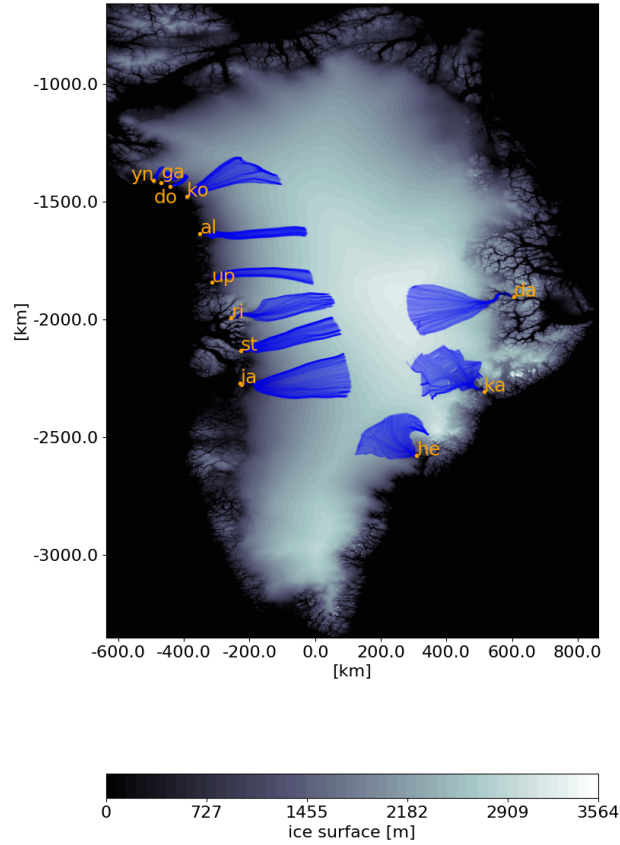
Figure 3. Terminus location (orange dot) with the catchment area (blue) of the twelve investigated glaciers: Alison Glacier (al), Daugaard-Jensen Glacier (da), Docker-Smith Glacier (do), Gade (ga) Helheim Glacier (he), Jakobshavn-Isbrae (ja), Kangerlussuaq Glacier (ka), Kong-Oscar Glacier (ko), Rink-Isbrae (ri), Store Glacier (st), Upernavik North Glacier (up), Yngvar-Nielsen Glacier (yn)
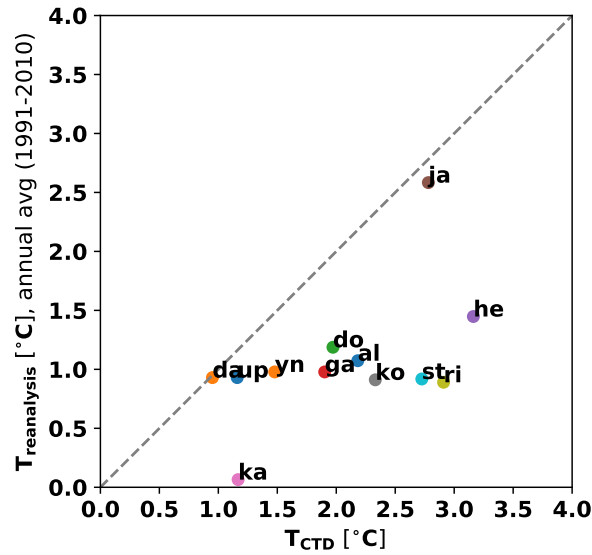
Figure 4. Temperature at the grounding line depth of CTD measurements closest to glacier front, inside the fjords (x-axis) and temperatures reconstructed from reanalysis data (y-axis) from the nearest possible grid-cell for all 12 glaciers: Alison (al), Daugaard-Jensen (da), Docker-Smith (do), Gade (ga), Helheim (he),Jakobshavn Isbrae (ji), Kangerlussuaq (ka), Kong Oscar (ko), Rink Isbrae (ri), Store (st), Upernavik (up), Yngvar Nielsen (yn).
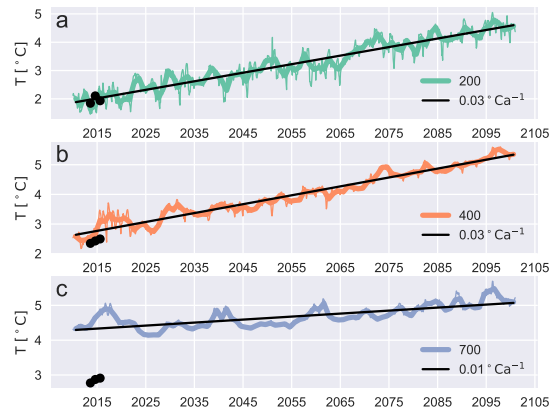
Figure 5. Monthly ocean temperature and centennial trend from the CMIP5 model MPI-ESM-LR in the closest grid-cells to the fjord of Rink Isbrae that have a depth of at least a) 200 m b) 400 m and c) 700 m depth. Black dots show CTD measurements at the same depth but inside the fjord.
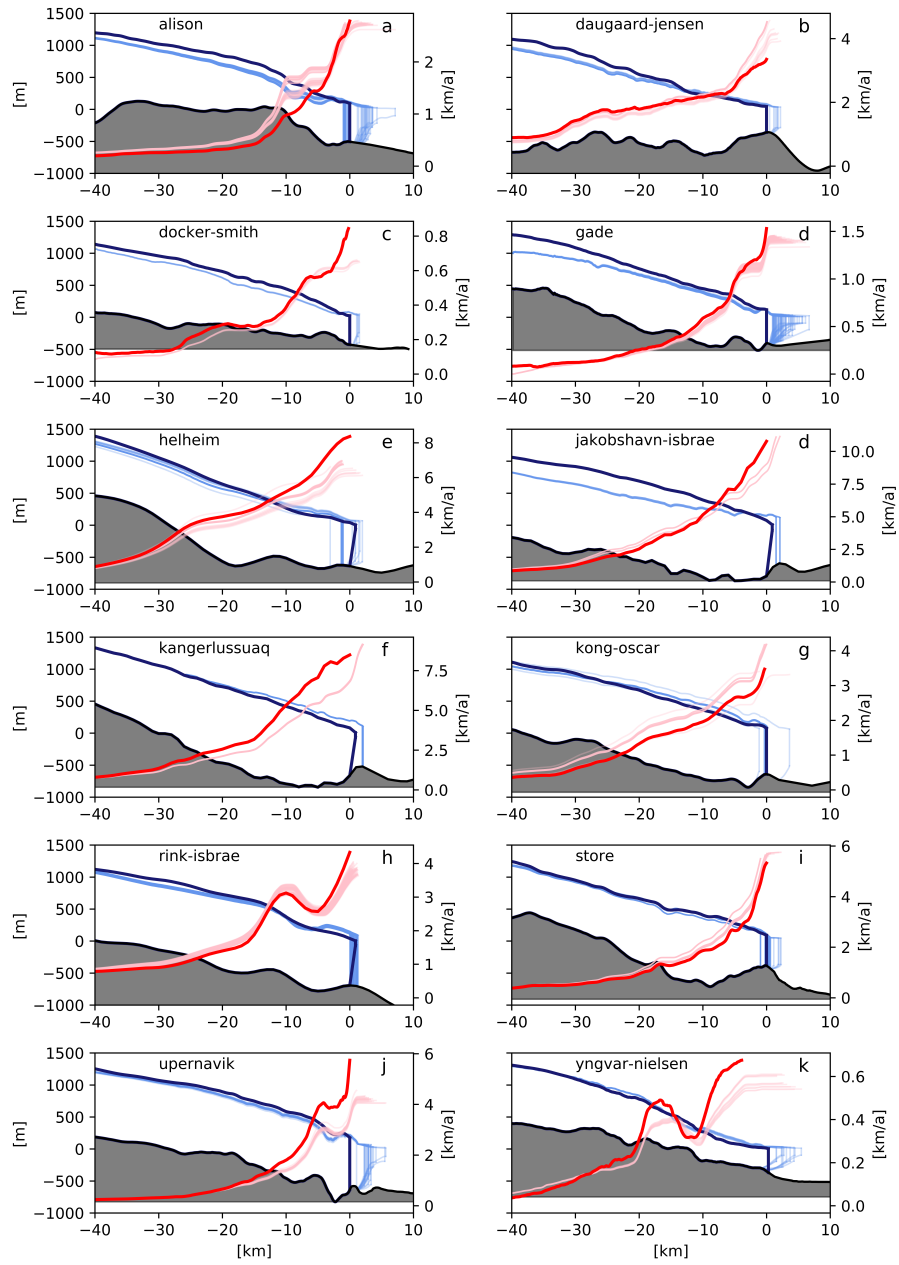
Figure 6. Simulated steady state after spin-up. Glacier elevation (light blue) and velocity profile (light red) for the last 40 km to the grounding line depicted together with observational data (dark blue and dark red) by Morlighem et al. (2014) and Rignot and Mouginot (2012). Bedrock data is derived by the flux weighted average over the whole catchment area. The number of simulations is given in Tab. S3, supporting information

.
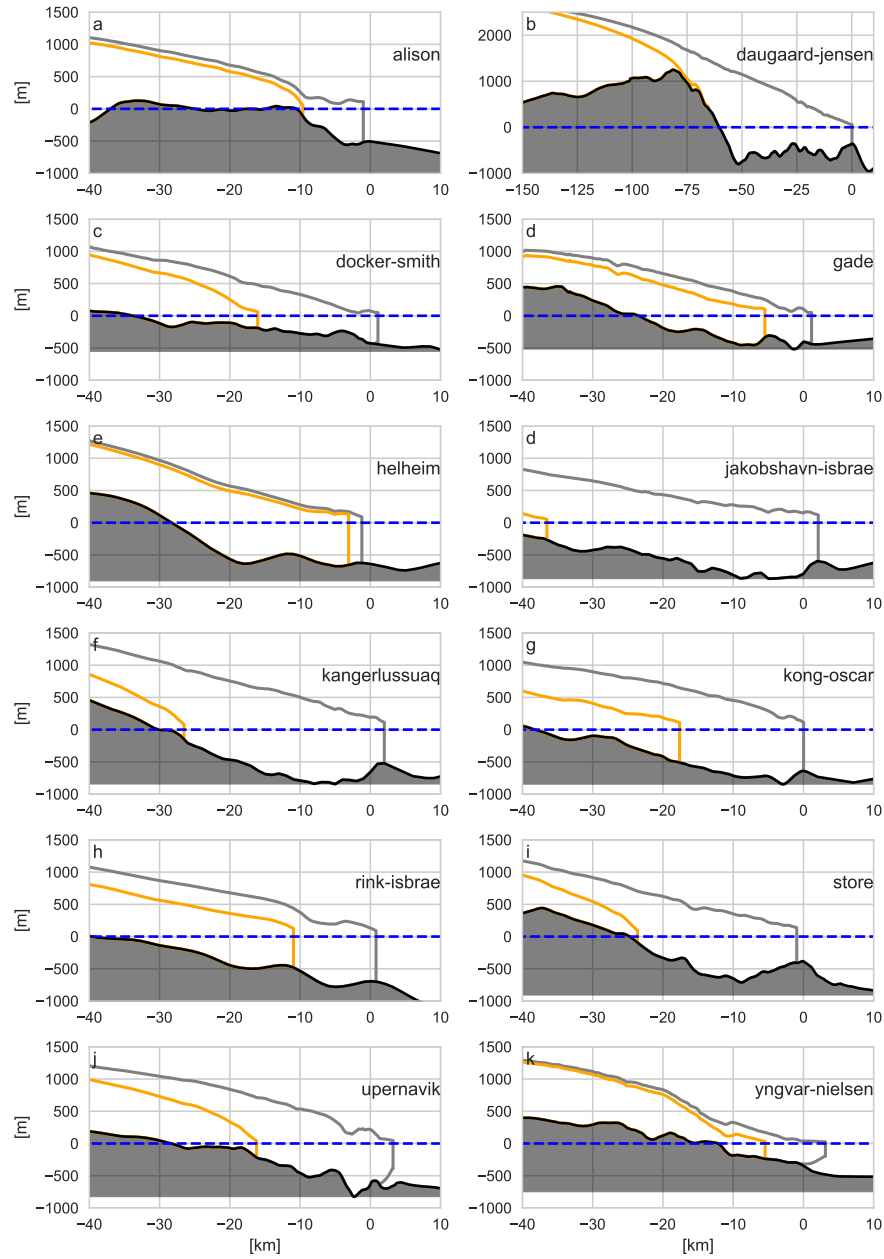
Figure 7. Retreat of median-range [3] SLR scenario for RCP 8.5 forcing scenarios (SMB and ocean temperature and subglacial discharge) for all 12 glaciers at 2100 (orange). Corresponding initial states are depicted in grey. Daugaard-Jensen, showed full retreat of over 60 km.

[3] median for an odd number of simulations, the first value of higher half for an even number of simulation
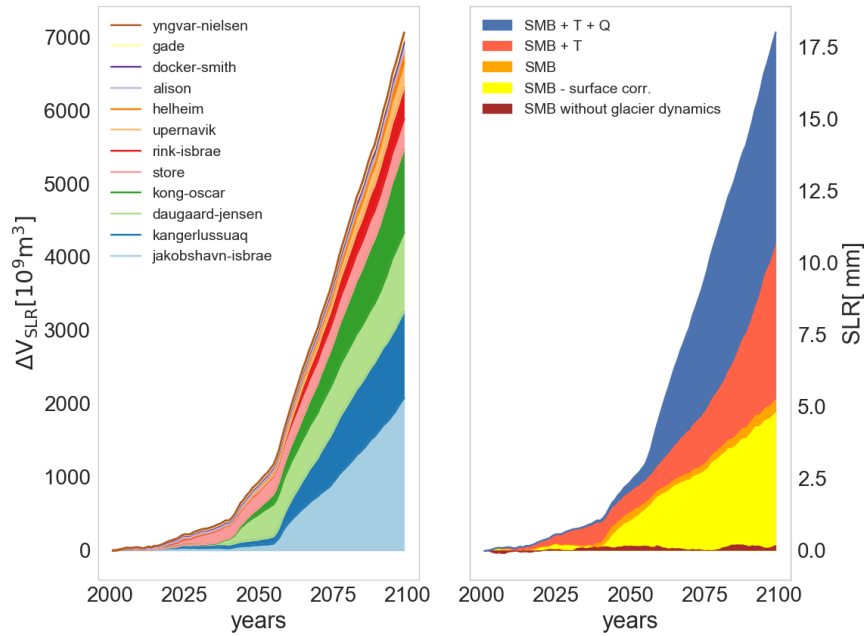
Figure 8. Cumulative sea level rise of median-range[3] SLR scenario from Fig. 7 for all 12 glaciers. Left panel: Individual glaciers' response to complete future forcing scenario (SMB, subglacial discharge Q and ocean temperature T). Right panel: The role of individual forcing factors for all glaciers. The dynamics response of all twelve glacier forced by $\mathrm{SMB} + \mathrm{T} + \mathrm{Q}$ (blue), $\mathrm{SMB} + \mathrm{T}$ (pink), SMB forcing only (orange) and SMB without the surface elevation feedback in the glacier model (yellow). The 'static' cumulative SMB anomaly over fixed present-day glacier domains and surface heights from MAR for all twelve glaciers (brown).

[3] median for an odd number of simulations, the first value of higher half for an even number of simulation
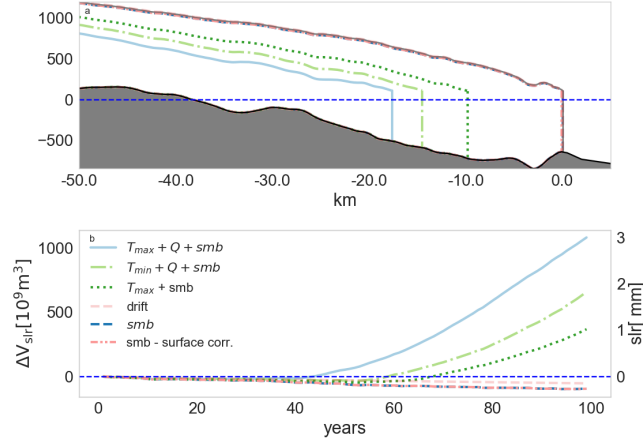
Figure 9. a) Kong-Oscar Glacier with a representative medium-slr retreat scenario applying forcing factors as subglacial discharge Q, ocean temperature T, surface mass balance smb with and without accounting for surface elevation correction (smb - surface corr.) for the medium SLR scenario. The corresponding SLR of each experiment is displayed in panel b).
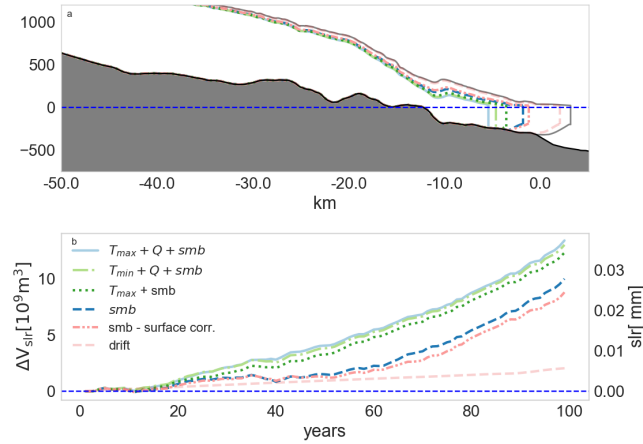
Figure 10. a) Yngvar Nielsen Glacier with a representative medium-slr retreat scenario applying forcing factors as subglacial discharge Q, ocean temperature T, surface mass balance smb with and without accounting for surface elevation correction (smb - surface corr.) for the medium SLR scenario. The corresponding SLR of each experiment is displayed in panel b).
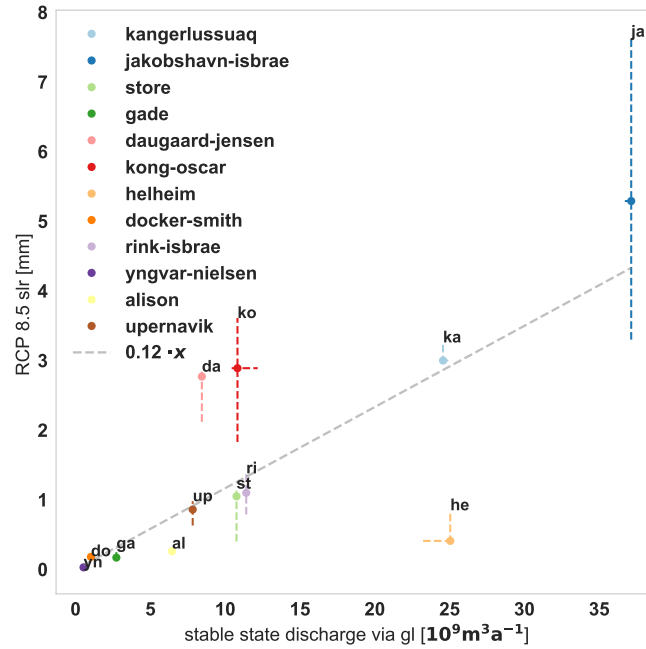
Figure 11. First to third quartile (median indicated with a dot) of contribution to SLR at 2100 under RCP 8.5 for each glacier from Table 3 as a function of the present-day grounding line discharge. The future simulations were forced by changes in SMB, subglacial discharge and minimal and maximal ocean temperature trend (Tab. 1). Grey dashed line indicates a linear regression obtained with an ordinary least square method from the median values. Slope and p-value are $0.12 \, \mathrm{mm \, km^{-3} \, a}$ and $9 \cdot 10^{-5}$, respectively. The correlation coefficient is 0.74.
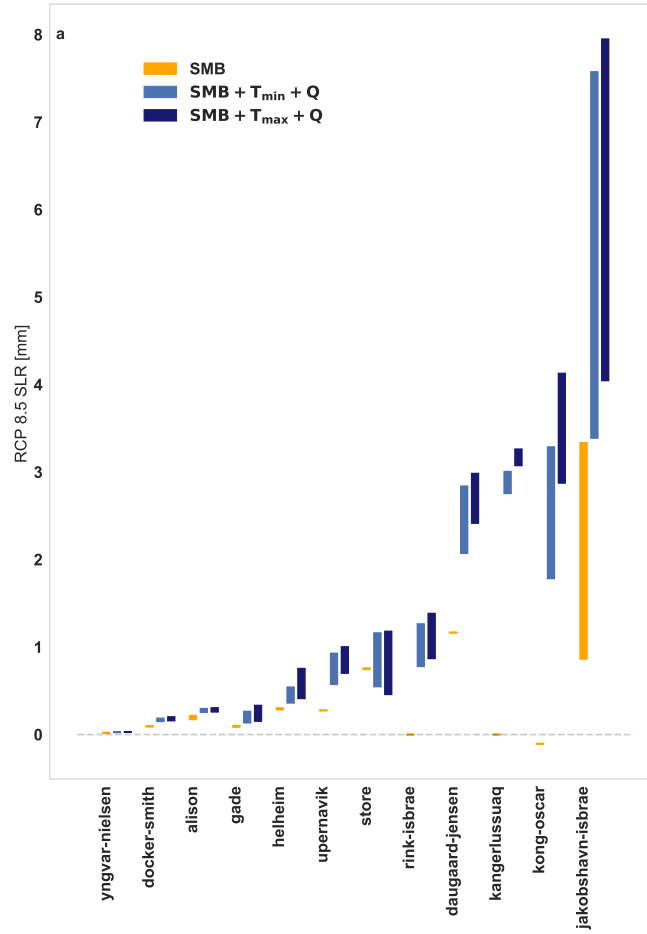
Figure 12. First to third quartile of contribution to SLR for each glacier. Future RCP 8.5 scenarios were either forced with SMB changes only (orange) or changes in SMB, ocean temperature (T_{min} and T_{max}) and subglacial discharge (blue).
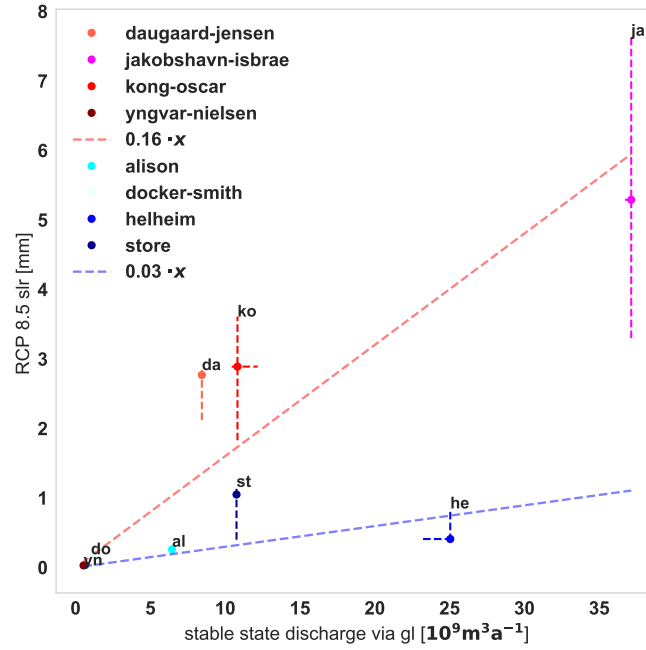
Figure 13. First to third quartile (median indicated with a dot) of contribution to SLR under RCP 8.5 for 8 glaciers from Table 3 as a function of the present-day grounding line discharge. The future simulations were forced by changes in SMB, subglacial discharge and minimal and maximal ocean temperature trend (Tab. 1). Dashed lines indicate a linear function of the present-day grounding line discharge in future SLR for 2100 obtained with an ordinary least square model from the median values for 4 glaciers only that result in a high slope (reddish colors) and that result in a low slope (blueish colors). For the redish glaciers, the resulting slope and p-value are $0.03 \, \mathrm{mm \, km^{-3}} \, \mathrm{a}$ and 0.18 respectively, and for the blueish glaciers $0.16 \, \mathrm{mm \, km^{-3}} \, \mathrm{a}$ and 0.01.

Table 1. Minimal and maximal ocean temperature trend (rounded to nearest degree Celsius) over 100 years for three CMIP5 Models derived from the grid-cells closest to each glacier fjord with minimum 400m depth. Detailed information are listed in Table S1, supporting information.

glacier name	$\Delta T_{\min}(^\circ\text{C}/100\text{a})$	$\Delta T_{\max}(^\circ\text{C}/100\text{a})$
Daugaard-Jensen	3	5
Helheim Glacier	2	3
Jakobshavn Isbae	2	4
Kangerlussuaq Glacier	3	4
Rink Isbrae	1	3
Store Glacier	1	3
Kong Oscar Glacier	1	3
Alison Glacier	1	3
Upernavik Isstrom	1	3
Yngvar Nielsen	1	3
Docker Smith Glacier	1	3
Gade Glacier	1	3

Table 2. Each investigated glacier with the mean grounding line discharge from observation $\mathrm{Flx}_{\mathrm{gl}}^{\star\mathrm{E}}$ (Enderlin and Howat, 2013) and from the stable state simulations $\mathrm{Flx}_{\mathrm{gl}}$ as well as the number of stable simulations (#). The melt flux range for floating termini from all present-day simulations $\mathrm{MeltFlx}$ and from the observational data $\mathrm{MeltFlx}^{\star\mathrm{E}}$ is calculated with the error ranges in Enderlin and Howat (2013) but with the condition $0 < \mathrm{MeltFlx}^{\star\mathrm{E}} < \mathrm{Flx}_{\mathrm{gl}}^{\star\mathrm{E}}$. The respective ratio of melt flux /grounding line discharge ($\mathrm{MeltFlx}/\mathrm{Flx}_{\mathrm{gl}}$) in % is listed for the simulation and observations ($^{\star E}$) and indicates how much ice that flows over the grounding line is lost by submarine melting. The sign * indicates glaciers for which the melt rate partition of the simulation does not overlap with the range of Enderlin and Howat (2013). Melt fluxes are derived for floating tongues and thus $\mathrm{MeltFlx} = 0$ indicates tidewater glaciers (no floating tongue). Store Glacier is not examined in Enderlin and Howat (2013).

glacier	$\mathrm{Flx}_{\mathrm{gl}}^{\star\mathrm{E}}$ 10^9 [m^3/a]	$\mathrm{Flx}_{\mathrm{gl}}$ 10^9 [m^3/a]	$\mathrm{MeltFlx}^{\star\mathrm{E}}$ 10^9 [m^3/a]	$\mathrm{MeltFlx}$ 10^9 [m^3/a]	$\mathrm{MeltFlx}^{\star\mathrm{E}}/\mathrm{Flx}_{\mathrm{gl}}^{\star\mathrm{E}}$ [%]	$\mathrm{MeltFlx}/\mathrm{Flx}_{\mathrm{gl}}$ [%]	#
alison	6.83	6.25 - 6.55	0.82 - 6.41	0.00 - 4.77	12 - 94	0 - 76	54
daugaard-jensen*	9.34	7.82 - 8.44	4.12 - 9.34	0.00 - 2.06	44 - 100	0 - 26	22
docker-smith	1.06	1.05 - 1.07	0.00 - 0.87	0.22 - 0.66	0 - 82	21 - 62	5
gade	4.85	2.63 - 2.81	0.00 - 4.85	0.17 - 2.14	0 - 100	6 - 77	55
helheim	29.16	22.84 - 25.94	0.19 - 6.90	0.00 - 8.39	1 - 24	0 - 36	28
jakobshavn-isbrae*	43.03	36.81 - 37.14	21.11 - 32.91	0.00 - 0.00	49 - 76	0 - 0	11
kangerlussuaq	38.80	24.51 - 24.58	0.00 - 6.83	0.00 - 0.00	0 - 18	0 - 0	39
kong-oscar	11.86	10.34 - 12.86	3.06 - 6.28	0.00 - 2.64	26 - 53	0 - 26	16
rink-isbrae	10.95	11.20 - 11.73	0.00 - 6.85	0.00 - 0.00	0 - 63	0 - 0	64
store	-	10.55 - 11.29	-	0.00 - 1.73	-	0 - 16	67
upernavik north	17.12	7.48 - 7.84	5.81 - 11.20	0.03 - 5.92	34 - 65	0 - 78	21
yngvar-nielsen	0.69	0.53 - 0.56	0.00 - 0.69	0.08 - 0.42	0 - 100	15 - 76	11

Table 3. Median, first and third quartile of SLR contribution from each glacier under RCP 8.5 scenario (SMB, subglacial discharge and ocean temperature (min and max)). Values are corrected from drift.

glacier	slr [mm]		
	median	first quartile	third quartile
alison	0.26	0.26	0.30
daugaard-jensen	2.73	2.12	2.84
docker-smith	0.18	0.15	0.19
gade	0.17	0.14	0.30
helheim	0.41	0.38	0.85
kangerlussuaq	3.00	2.96	3.26
kong-oscar	2.89	1.83	3.61
rink-isbrae	1.10	0.79	1.38
store	1.05	0.40	1.16
upernavik	0.85	0.63	0.98
yngvar-nielsen	0.03	0.03	0.03
jakobshavn-isbrae	5.22	3.30	7.65
sum	17.90	12.99	22.55

Table 4. Median, first and third quartile of grounding line retreat from each glacier under RCP 8.5 scenario (SMB, subglacial discharge and ocean temperature (min and max)). Values are corrected from drift.

glacier	grounding line retreat [km]		
	median	first quartile	third quartile
alison	9.21	8.69	10.77
daugaard-jensen	60.80	28.99	62.21
docker-smith	15.13	14.23	16.49
gade	5.85	4.62	15.17
helheim	1.52	1.10	9.63
kangerlussuaq	28.52	28.44	28.53
kong-oscar	17.65	14.61	18.63
rink-isbrae	11.07	10.90	11.18
store	17.59	3.99	23.21
upernavik	17.43	12.79	17.72
yngvar-nielsen	4.69	4.28	5.22
jakobshavn-isbrae	38.57	19.85	40.53
avg	19.00	12.71	21.61